Summer 2022

Structure Preserving Reduced-Order Models of Hamiltonian Systems

Megan Alice McKay

Structure Preserving Reduced-Order Models of Hamiltonian Systems

by

Megan Alice McKay

Bachelor of Science
Millersville University of Pennsylvania 2019

Submitted in Partial Fulfillment of the Requirements

for the Degree of Master of Science in

Mathematics

College of Arts and Sciences

University of South Carolina

2022

Accepted by:

Zhu Wang, Director of Thesis

Hong Wang, Reader

Tracey L. Weldon, Vice Provost and Dean of the Graduate School

Abstract

Large-scale dynamical systems are expensive to simulate due to the computational cost accrued y the substantial number of degrees of freedom. To accelerate repeated numerical simulations of the systems, proper orthogonal decomposition reduced order models (POD-ROMs) have been developed. When applied to Hamiltonian systems, however, special care must be taken when performing the reduced order modeling to keep their energy-preserving nature. This work presents a survey of several structure-preserving reduced order models (SP-ROMs). In addition, this work employs the discrete empirical interpolation method (DEIM) and develops an SP-DEIM model for nonlinear Hamiltonian systems. The wave equation is considered as a test bed for the proposed SP-ROMs.

Results show that a model using shifted snapshots to generate a POD basis (SP-ROM-2) is able to produce an exact Hamiltonian. In addition, it is shown that the SP-DEIM model is able to produce similar results with a nonlinear system as the SP-ROM-1 given a linear system.

Table of Contents

Abstract iii

List of Tables vi

List of Figures vii

Chapter 1 Introduction 1

1.1 Reduced Order Models 3

1.2 Hamiltonian Systems 6

1.3 Reduced Order Models for Hamiltonian Systems 7

Chapter 2 Full Order Model 9

2.1 Fully Discrete Hamiltonian System 9

2.2 Numerical Experiments 12

Chapter 3 Reduced Order Model 16

3.1 POD Reduced Order Modeling 16

3.2 POD-ROM for Hamiltonian Systems 20

3.3 Numerical Experiments 21

Chapter 4 Structure Preserving Reduced Order Model 25

4.1 SP-ROM for Hamiltonian Systems 25

4.2 Numerical Experiments 26

Chapter 5 Structure Preserving Nonlinear Reduced Order Model 36

5.1 SP-DEIM for Hamiltonian Systems 36

5.2 Numerical Experiments 38

Chapter 6 Conclusion 47

Bibliography 48

List of Tables

Table 2.1 Full Order Model Error in Time 15

Table 2.2 Full Order Model Error in Space 15

List of Figures

Figure 2.1 Full order model simulation: time evolution of u and v 14

Figure 2.2 A well preserved Hamiltonian generated by the full order model simulation 14

Figure 3.1 Visual representation of reduced order model 17

Figure 3.2 Linear wave reduced order model Hamiltonian error results for $r = 5$ (left) and $r = 20$ (right) 22

Figure 3.3 Linear wave reduced order model u error for $r = 5$ (top) and $r = 20$ (bottom) 23

Figure 3.4 Linear wave reduced order model v error for $r = 5$ (top) and $r = 20$ (bottom) 24

Figure 4.1 SP-ROM-0: Hamiltonian error plots for $r = 5$ (left) and $r = 20$ (right). 27

Figure 4.2 SP-ROM-0: u error plots for $r = 5$ (top) and $r = 20$ (bottom). . . 28

Figure 4.3 SP-ROM-0: v error plots for $r = 5$ (top) and $r = 20$ (bottom). . . 29

Figure 4.4 SP-ROM-1: Hamiltonian error plots for $r = 5$ (left) and $r = 20$ (right). 30

Figure 4.5 SP-ROM-1: u error plots for $r = 5$ (top) and $r = 20$ (bottom). . . 31

Figure 4.6 SP-ROM-1: v error plots for $r = 5$ (top) and $r = 20$ (bottom). . . 32

Figure 4.7 SP-ROM-2: Hamiltonian error plots for $r = 5$ (left) and $r = 20$ (right). 33

Figure 4.8 SP-ROM-2: u error plots for $r = 5$ (top) and $r = 20$ (bottom). . . 34

Figure 4.9 SP-ROM-2: v error plots for $r = 5$ (top) and $r = 20$ (bottom). . . 35

Figure 5.1 SP-DEIM-1: Hamiltonian errors for $r = 5$ (top) and $r = 20$ (bottom). 41

Figure 5.2 SP-DEIM-1: u error plots for $r = 5$ (top) and $r = 20$ (bottom). . 42

Figure 5.3 SP-DEIM-1: v error plots for $r = 5$ (top) and $r = 20$ (bottom). . 43

Figure 5.4 SP-DEIM-2: Hamiltonian errors for $r = 5$ (top) and $r = 20$ (bottom). 44

Figure 5.5 SP-DEIM-2: u error plots for $r = 5$ (top) and $r = 20$ (bottom). . 45

Figure 5.6 SP-DEIM-2: v error plots for $r = 5$ (top) and $r = 20$ (bottom). . 46

Chapter 1

Introduction

Mathematical modeling is the act of observing the complex world and attempting to capture these dynamics with a mathematical formula. Due to the intricacies that abound in the everyday, the mathematical models could be complicated and the numerical methods used to simulate such models can become extremely computationally expensive. In the applications of optimization and optimal control, this issue becomes even more apparent when repeated simulations of these expensive computations are required. To reduce their computational complexity, model order reduction has been developed which generates a surrogate model, diminishing the number of degrees of freedom in the system. In general, this process creates a low-dimensional offline model which can be computed more efficiently during the online stage. Unfortunately, a loss of stability or accuracy is a typical cost of improving computational efficiency. Hence, much attention has been directed to research in developing methods that reduce computational costs while maintaining high levels of accuracy for certain types of systems. Some examples of situations that elicit model reduction can be found in heat transfer [10], fluid dynamics [6, 49], chemical reactions [54] or biological systems [2]. For a detailed discussion on model order reduction, the reader is referred to [7, 11, 1, 28].

Note that these observed dynamical systems are governed by a system of partial differential equations (PDEs) or a large system of ordinary differential equations (ODEs). To illustrate the methodology of model order reduction, we let $\mathbf{y}(x,t)$, with the spatial variable $x \in \Omega$ and the time variable $t \in (t_0, t_0+T)$, be the state variables

in the original system and $\mathcal{H}$ be a Hilbert space. This system reads, find $\mathbf{y}(\cdot, t) \in \mathcal{H}$ satisfying

$$\begin{cases} \frac{\partial y}{\partial t}(\cdot, t) = \mathbf{f}(t, y(x, t)) \\ y(x, t_0) = y_0(x), \end{cases} \tag{1.1}$$

together with some boundary conditions. Due to possible nonlinearity of the equation, and complicated geometrical domain, it is usually impossible to find analytic solutions. For this reason, numerical solutions to (1.1) are sought which satisfy a discrete ODE system. To achieve this, prominent numerical methods such as finite difference, finite volume, or finite element methods can be applied. Then, instead of the PDE system that has an infinite number of degrees of freedom, the discrete system involved a finite, but possibly large, number of degrees of freedom. It reads, find $\mathbf{y}(\cdot, t) \in \mathbb{R}^N$ satisfying

$$\begin{cases} \mathbf{y}'(x, t) = \mathbf{f}(t, \mathbf{y}(x, t) \\ \mathbf{y}(x, t_0) = \mathbf{y}_0(x). \end{cases} \tag{1.2}$$

When the discrete system (1.2), also referred to as the full-order model (FOM), is extremely large-scale, as is the case of many real-world engineering problems, the high-fidelity simulations are time-consuming. In addition, many real-world applications such as optimal control or optimization problems in scientific computing require a system to be simulated repeatedly which makes the use of full-order simulations prohibitive in practice. Such challenges encountered in control problems are discussed in [9, 41, 49]. Model order reduction has been developed to help mitigate these challenges by seeking a low-dimensional model to represent the full-order model.

Generally speaking, the model reduction determines a handful of reduced bases to approximate the solution manifold, then constructs a low-dimensional surrogate of the FOM, (1.1) or (1.2). This surrogate is called the reduced-order model (ROM) which is a system of ODEs of significantly smaller size compared to the FOM. Due to its small

size, it can then be solved quickly (with special treatment applied to the nonlinear terms), and therefore can replace the original model during the online stage. While building the low-dimensional model may be expensive, these costs are accrued in the offline phase, which is distinct from the repeated online full-order simulations. Several different approaches have been developed for constructing a ROM such as proper orthogonal decomposition, dynamical model decomposition, and balanced truncation [7]. In this work, we will focus on the proper orthogonal decomposition (POD) approach since it can be easily applied to nonlinear time-dependent systems.

1.1 Reduced Order Models

Depending on how the ROMs are constructed, the reduced order models can be classified into two categories: projection-based and data-driven approaches. The former builds the low-dimensional model based on the projection of the FOM to the reduced basis subspace, requiring the FOM information; while the latter is purely data-driven, without accessing the FOM information

Projection-based reduced order modeling

In the survey paper [7], Benner et al. gather a large amount of the current research works for projection-based models. Applications for these model reduction techniques range from aeroelasticity [3], to interconnect synthesis [35, 17], to semiconductors [25]. Previous work in such fields has focused on several methods of optimization, optimal control, and uncertainty quantification. In [46], the reduced basis method is combined with trust region optimization to manage the ROMs. *A posteriori* error bounds are presented and used to guarantee convergence and optimally distribute the FOM ad ROM runs. The results determined that the number of FOM solves necessary was drastically reduced thanks to this combination [46].

The optimality system POD (OS-POD), proposed in [33], utilizes the optimality

conditions in the derivation of the POD model in the context of optimal control. This method circumvents the issue of unmodelled dynamics in the POD approach to optimal control. The feasibility of this approach was then tested against the basic POD solved for a fixed control using sequential quadratic programming (SQP) as well as an FE-SQP approach, where a preconditioned generalized minimal residual (GMRES) method is used to carry out the SQP inexactly. The results showed that there exists a drastic difference in the POD basis functions between the initial and optimized bases [33].

Another area in which projection-based ROMs have been utilized is in uncertainty quantification. In [12], Bui-Thanh et al. consider a computational fluid dynamics (CFD) model to address the input uncertainties by random sampling methods such as the Monte Carlo. This approach can require thousands of CFD solves, which does not make the data readily available for practical applications. Therefore, linearized CDF-ROMs are developed that can accurately reproduce the CFD Monte Carlo simulation with a significant reduction in computational cost [12].

Data-Driven Reduced Order Modeling

Several successful data-driven model reduction approaches are outlined in [51]. For example, the Loewner framework in [29] uses multivariate rational interpolation, the barycentric form, and Lowener matrices to build ROMs. This approach introduces the new ability to choose individual reduced orders for each parameter, increasing its effectiveness. In [38], the Eigensystem Realization Algorithm (ERA) is used to obtain the ROM directly from the data. This is useful for several reasons, notably when the data from adjoint simulations is unavailable to properly balance a POD-ROM. It was found that the algorithm significantly improves computational efficiency.

Quadrature-based fitting is yet another method, employed in [18], where the original vector fitting is improved by properly weighting the well-chosen sampling points

based on quadrature rules. This modification helps recover the original transfer function with better accuracy as measured by the H_2 norm. While [23] and [5] have both extended the Loewner approach to bilinear and quadratic-bilinear systems, data-driven approaches for nonlinear systems is an area of growing interest.

An operator inference approach infers approximations of the reduced operators without requiring the full-model operators [45]. These inferred operators converge in the Frobenius norm to the reduced operators that would have been obtained intrusively. The numerical results demonstrated the operator inference on a tubular reactor model with a polynomial nonlinear term of the third order.

Lifting transformations have allowed this operator inference framework to extend to general nonlinear systems. In [52], machine learning introduces the flexibility to use transformed physical variables to define the POD basis instead of the traditional physical variables of the high-fidelity code. This method has been used to learn a quadratic ROM from transformed snapshot data and was shown to be predictive 200% past the training interval. This approach has also been extended in [8] where a gray-box setting is utilized. This method uses analytical expressions for the nonpolynomial nonlinear terms and the rest of the operators are learned via inference. Benner et al. demonstrate the method on three problems governed by PDEs, namely the diffusion-reaction Chafee-Infante model, a tubular reactor model for reactive flows, and a batch-chromatography model [7]. The numerical results show comparable accuracy to models constructed with successful intrusive model reduction methods.

In [44], Peherstorfer et al. demonstrate how to obtain re-projected trajectories of high-dimensional systems in low-dimensional subspaces. His numerical results demonstrate that the proposed models match the reduced models formulated from traditional model reduction. The results confirm that low-dimensional models fitted with re-projected trajectories are accurately predictive even in situations where typical models fail. In another paper, Peherstorfer et al. construct non-Markovian

reduced models to make future-state predictions that are based on the history of the states [53]. This approach uses partially observed states from high-dimensional systems. The results show that this approach learns non-Markovian reduced models with only 20% observed state data that are similar in accuracy to the traditional Markovian models fitted with 99% observed components.

1.2 Hamiltonian Systems

For the evolution system, Hamiltonian formulation is important as it provides critical insights into the dynamics which has been widely used in physical systems such as a planetary system or an electron in an electromagnetic field. A classic Hamiltonian system is a dynamic system of differential equations defined by Hamilton's equations:

$$\begin{cases} \frac{dp}{dt} = -\nabla_q H \\ \frac{dq}{dt} = \nabla_q H, \end{cases} \tag{1.3}$$

where p is the momentum in phase space, q is the position in phase space, and $H(q, p, t)$ is the Hamiltonian function of the system [50]. Because of the geometric structure of the system, the Hamiltonian is constant along the integral curves, which reflects the conservation of energy in the physical setting.

To numerically solve the Hamiltonian system, it is first reduced to a system of ODEs. Specific structure-preserving spatial discretization is derived to maintain the intricate characteristics of a Hamiltonian system. Next, a geometric time integration must take place to preserve the structure as time evolves. Because of these delicacies, not all well-known numerical methods can be used on Hamiltonian systems. In fact, several modifications must be implemented to create models that preserve the structure of these Hamiltonian systems. For more discussion on these modifications, the reader is referred to [19].

1.3 Reduced Order Models for Hamiltonian Systems

Although proper orthogonal decomposition reduced-order models (POD-ROMs) have been successfully applied in many engineering problems, when Hamiltonian systems on considered, direct use of these methods cannot preserve the structure of the system. A significant amount of research has been conducted on how to modify models to account for structure preservation. Both projection-based and data-driven approaches are considered.

Projection-based models reduce the FOM by restricting the solution to a subspace of the reduced basis space, therefore reducing the number of equations [4]. In a paper by Gong et al., a modified Galerkin POD-ROM was developed to overcome this discrepancy [22]. Another example of structure-preserving research is in the area of neural networks. In [24], Hamiltonian neural networks (HNNs) were designed which are able to learn problems where the preservation of the structure is necessary. Two new classes of symplectic networks, the LA-SympNets, and the G-SympNets, were proposed in [29] where the former is composed of linear and nonlinear activation modules and the latter of gradient modules. It was proven that SympNets can approximate arbitrary symplectic maps and even small SympNets are able to handle Hamiltonian systems with data points from any size time steps. In [21], A Bayesian probabilistic formulation is proposed. An approximate marginal Markov Chain Monte Carlo algorithm is used to discover a Hamiltonian from data. This procedure outperforms the existing methods by utilizing the symplecticness of the Hamiltonian as well as implementing a learning objective that accounts for several features such as unknown parameters, model form, and measurement noise.

A non-intrusive physics-preserving method was designed in [51] that learns ROMs of canonical Hamiltonian systems. The method exploits knowledge of the Hamiltonian function to parameterize a Hamiltonian ROM which can then be learned from data projected via symplectic projectors. This model is gray-box as it utilizes knowledge

of the Hamiltonian structure at the continuous level, as well as knowledge of spatially local components in the system, however, access to computer code for the FOM is not assumed.

Chapter 2

Full Order Model

2.1 Fully Discrete Hamiltonian System

In this work, we will focus on general Hamitonian systems that are governed by the following evolutionary PDEs, with the appropriate initial and boundary conditions:

$$\dot{u} = \mathcal{D}\frac{\delta \mathcal{H}}{\delta u}, \tag{2.1}$$

where independent variables $(x, t) \in \Omega \subset \mathbb{R}^d \times \mathbb{R}$, and u that belong to a Hilbert space $\mathcal{B}$, $\mathcal{D}$ is a constant linear differential operator, and $\dot{u} = \frac{\partial u}{\partial t}$. The Hamiltonian

$$\mathcal{H}[u] = \int_\Omega H(x; u)dx \tag{2.2}$$

where $dx = d_1 dx_2 \cdots dx_d$. The variational derivative of $\mathcal{H}$ is given by $\frac{\delta \mathcal{H}}{\delta u}$ satisfying.

$$\frac{d}{d\epsilon}\mathcal{H}[u + \epsilon v]\Big|_{\epsilon=0} = \left\langle \frac{\delta \mathcal{H}}{\delta u}, v \right\rangle$$

for all $u, v \in \mathcal{B}$ [43].

We follow a discussion from [13] and begin by considering Hamiltonian systems of the form (2.1) where $\mathcal{D}$ is a constant, skew-adjoint operator and $\mathcal{H}$ represents the total energy [43]. Since $\mathcal{D}$ is skew-adjoint with respect to the L_2 norm, that is,

$$\int_\Omega u\mathcal{D}udx = 0, \quad \forall u \in \mathcal{B}, \tag{2.3}$$

the system is energy-conservative. This is because the system (2.1) has the time derivative of the Hamiltonian to be zero: $\dot{\mathcal{I}} = \int_\Omega \frac{\delta \mathcal{I}}{\delta u}\mathcal{S}\frac{\delta \mathcal{H}}{\delta u}dx = 0$.

The other possible case for PDEs of type (2.1) is when $\mathcal{D}$ is a constant negative (semi)definite operator with respect to the L^2 inner product. This gives

$$\int_\Omega u\mathcal{D}udx \leq 0, \quad \forall u \in \mathcal{B}. \tag{2.4}$$

In this scenario, $\mathcal{H}$ is a Lyapunov function and the system is energy-dissipative.

In this work, we will focus on the system of the first type. With appropriate discretization in space, it can be put in the following semi-discrete form:

$$\dot{\mathbf{u}} = \overline{\mathcal{D}}\nabla\overline{\mathcal{H}}(\mathbf{u}), \qquad \overline{\mathcal{D}}^\top = -\overline{\mathcal{D}}, \qquad \mathbf{u} \in \mathbb{R}^N. \tag{2.5}$$

Here, the discrete operator is denoted by the bars, $\overline{\mathcal{D}}$ is skew-symmetric, and $\overline{\mathcal{H}} : \mathbb{R}^N \to \mathbb{R}$ is chosen in a way that lets $\overline{\mathcal{H}}\Delta x$ be an approximation to $\mathcal{H}$.

To fully discretize the system (2.1), a time integration also needs to take place. Among the geometric integration methods, the average vector field (AVF) method, which was introduced by Quispel in [47], could preserve the energy $\overline{\mathcal{H}}$ exactly for any vector field f of the form $f(\mathbf{u}) = \overline{\mathcal{D}}\nabla\overline{\mathcal{H}}(\mathbf{u})$. The AVF method is related to discrete gradient methods and is set apart by its ability to preserve linear symmetries and simplicity, among other characteristics [13, 39]. Take Newton's laws of motion, for example, we have

$$\mathbf{x}^*_{n+1} = \mathbf{x}_n + \int_{t_n}^{t_{n+1}} \mathbf{v}(t)dt \tag{2.6}$$

$$\mathbf{v}^*_{n+1} = \mathbf{v}_n + \mathbf{M}^{-1}\int_{t_n}^{t_{n+1}} \mathbf{f}(\mathbf{x}(t))dt \tag{2.7}$$

where $\mathbf{x}_n \in \mathbb{R}^m$, and $\mathbf{v}_n \in \mathbb{R}^m$ reflect the positions and velocities in time t_n and $\mathbf{x}^*_{n+1} \in \mathbb{R}^m$, and $\mathbf{v}^*_{n+1} \in \mathbb{R}^m$ represent the ground truth solutions in time t_{n+1}. In addition, according to Newton's laws of motion, $\mathbf{x} : \mathbb{R} \to \mathbb{R}^m$ and $\mathbf{v} : \mathbb{R} \to \mathbb{R}^m$ give the exact trajectories of the positions and velocities, where $\mathbf{f} : \mathbb{R}^m \to \mathbb{R}^m$ are position-dependent forces and $\mathbf{M} \in \mathbb{R}^{m\times m}$ is the mass matrix. When we assume that $\mathbf{f}$ is conservative, then there exists potential energy $E : \mathbb{R}^m \to \mathbb{R}$ such that $\mathbf{f} = -\nabla E$ and the total energy is conserved: $E(\mathbf{x}_{n+1}) + \frac{1}{2}||\mathbf{v}_{n+1}||^2_{\mathbf{M}} = E(\mathbf{x}_n) + \frac{1}{2}||\mathbf{v}_n||^2_{\mathbf{M}}$, where $||\cdot||_{\mathbf{M}}$

denotes the mass-matrix norm, which represents the kinetic energy [48]. Because the trajectories $\mathbf{x}(t)$ and $\mathbf{v}(t)$ are unknown, the integrals given in equations (2.6) and (2.7) must be approximated numerically. The AVF method uses the following approximation:

$$\mathbf{x}_{n+1} = \mathbf{x}_n + h \int_0^1 [(1-t)\mathbf{v}_n + t\mathbf{v}_{n+1}]dt \tag{2.8}$$

$$\mathbf{v}_{n+1} = \mathbf{v}_n + h\mathbf{M}^{-1} \int_0^1 \mathbf{f}((1-t))\mathbf{x}_n + t\mathbf{x}_{n+1})dt \tag{2.9}$$

which replaces the unknown trajectories $\mathbf{x}(t)$ and $\mathbf{v}(t)$ with straight lines [48]. It can be shown that this approximation retains the exact energy conservation property as long as the equations (2.8) and (2.9) are evaluated exactly [47]. This is the necessary property that ensures the freedom of using the AVF method on the general Hamiltonian systems.

In [16], Cieśliński shows that the AVF method is of second order and presents two locally exact modifications to expand the method to third and fourth-order accuracy. The schemes were tested on circular orbits using simplified expressions for the AVF discrete gradients. The results showed that the h-dependence (time-step) of the error is practically linear and aligns nicely with the computed orders of the schemes. In [27], it is found that the AVF(2)-CFD (compact finite difference) scheme achieves second-order accuracy in time and fourth-order accuracy in space. In addition, the AVF(4)-CFD method had fourth-order accuracy in both time and space. Finally, a sixth-order AVF method was developed in [34] which shows slow linear growth of the solution error as well as good preservation of the discrete Hamiltonian. Next, we will give a concrete example of a Hamiltonian system and discuss the corresponding discrete system.

2.2 Numerical Experiments

Consider the one-dimensional semilinear wave equation with constant speed given by c,

$$u_{tt} = c^2 u_{xx}, \quad 0 \leq x \leq l \text{ and } 0 \leq t \leq T. \tag{2.10}$$

This equation can be cast into Hamiltonian form with the symplectic structure by using a spatial discretization with N degrees of freedom, which reads:

$$\begin{bmatrix} \dot{\mathbf{u}} \\ \dot{\mathbf{v}} \end{bmatrix} = \begin{bmatrix} 0 & \mathrm{I}_n \\ -\mathrm{I}_n & 0 \end{bmatrix} \begin{bmatrix} \mathbf{-Au} \\ \mathbf{v} \end{bmatrix}, \tag{2.11}$$

where $\mathbf{A}$ is a discrete, scaled, one-dimensional second-order differential operator with a three-point stencil. Consider the average vector field (AVF) method for time integration. Let $\mathbf{u}^k$ be the solution at the time step k and denote the right hand side of (2.11) by $\mathbf{f}(\cdot)$, the AVF method is as follows.

$$\frac{\mathbf{u}^{k+1} - \mathbf{u}^k}{\Delta t} = \int_0^1 \mathbf{f}((1-\xi)\mathbf{u}^k + \xi \mathbf{u}^{k+1}) d\xi. \tag{2.12}$$

Details for how this method conserves energy at each step can be found in [47] and error bounds are developed in [20]. Since our gradient system is symplectic, the AVF method is able to keep the Hamiltonian function constant.

After applying the AVF method with a time step of Δt, we obtain

$$\begin{bmatrix} \frac{\mathbf{u}^{k+1}-\mathbf{u}^k}{\Delta t} \\ \frac{\mathbf{v}^{k+1}-\mathbf{v}^k}{\Delta t} \end{bmatrix} = \begin{bmatrix} 0 & \mathrm{I}_n \\ -\mathrm{I}_n & 0 \end{bmatrix} \begin{bmatrix} -\mathbf{A}\frac{\mathbf{u}^{k+1}+\mathbf{u}^k}{2} \\ \frac{\mathbf{v}^{k+1}+\mathbf{v}^k}{2}, \end{bmatrix} \tag{2.13}$$

where A is a matrix given by

$$\mathbf{A} = \frac{c^2}{\Delta x^2} = \begin{bmatrix} -2 & 1 & 0 & 0 & \dots & 1 \\ 1 & -2 & 1 & 0 & \dots & 0 \\ & & \ddots & \ddots & \ddots & \\ 0 & \dots & 0 & 1 & -2 & 1 \\ 1 & \dots & 0 & 0 & 1 & -2 \end{bmatrix}. \tag{2.14}$$

Indeed, the system has

$$\frac{\mathbf{u}^{k+1}-\mathbf{u}^k}{\Delta t}=\frac{\mathbf{v}^{k+1}-\mathbf{v}^k}{2} \implies \mathbf{u}^{k+1}-\mathbf{u}^k=\frac{\Delta t}{2}(\mathbf{v}^{k+1}+\mathbf{v}^k) \tag{2.15}$$

and

$$\frac{\mathbf{v}^{k+1}-\mathbf{v}^k}{\Delta t}=\mathbf{A}\frac{\mathbf{u}^{k+1}-\mathbf{u}^k}{2}. \tag{2.16}$$

By plugging (2.15) into (2.16) we get

$$\frac{\mathbf{v}^{k+1}-\mathbf{v}^k}{\Delta t}=\mathbf{A}\frac{2\mathbf{u}^k+\frac{\Delta t}{2}(\mathbf{v}^{k+1}+\mathbf{v}^k)}{2}=\mathbf{A}\left[\mathbf{u}^k+\frac{\Delta t}{4}(\mathbf{v}^{k+1}+\mathbf{v}^k)\right]. \tag{2.17}$$

From (2.17) we have

$$\mathbf{v}^{k+1}-\mathbf{v}^k=\mathbf{A}\Delta t\mathbf{u}^k+\mathbf{A}\frac{\Delta t^2}{4}\mathbf{v}^{k+1}+\mathbf{A}\frac{\Delta t^2}{4}\mathbf{v}^k. \tag{2.18}$$

Hence, $\mathbf{v}^{k+1}$ satisfies:

$$\left(\mathrm{I}-\mathbf{A}\frac{\Delta t^2}{4}\right)\mathbf{v}^{k+1}=\mathbf{A}\Delta t\mathbf{u}^k+\left(\mathrm{I}+\mathbf{A}\frac{\Delta t^2}{4}\right)\mathbf{v}^k. \tag{2.19}$$

We then solve (2.19) for $\mathbf{v}^{k+1}$, which we then plug in to (2.15) to obtain $\mathbf{u}^{k+1}$.

As a numerical test, we choose $c=0.1$ and the initial condition $u_0=l(s(x))$ and $\dot{u}=0$ where $l(s)$ is a cubic spline function defined by

$$l(s)=\begin{cases}1-\frac{3}{2}s^2+\frac{3}{4}s^3 & 0\le s\le 1\\ \frac{1}{4}(2-s)^3 & 1<s\le 2\\ 0 & s\ge 2\end{cases}$$

with $s(x)=10|x-\frac{1}{2}|$. In the computational setting, we set $N=500$, $T=50$ and $\Delta t=0.01$ and obtain the results shown in figures 2.1 and 2.2. We note that the energy is well-preserved at the value of 0.07499. The simulation of the full order model CPU time takes about 6.4267 seconds using Matlab on a PC.

To measure the numerical errors of the methods, we use the maximum approximation error over the whole spatial-temporal domain. This is given by

$$\varepsilon_\infty=\max_{k\ge 0}\max_{0\le i\le N}\sqrt{[(\mathbf{u}^k)_i-(\mathbf{u}^k_{ref})_i]^2+[(\mathbf{v}^k)_i-(\mathbf{v}^k_{ref})_i]^2}.$$

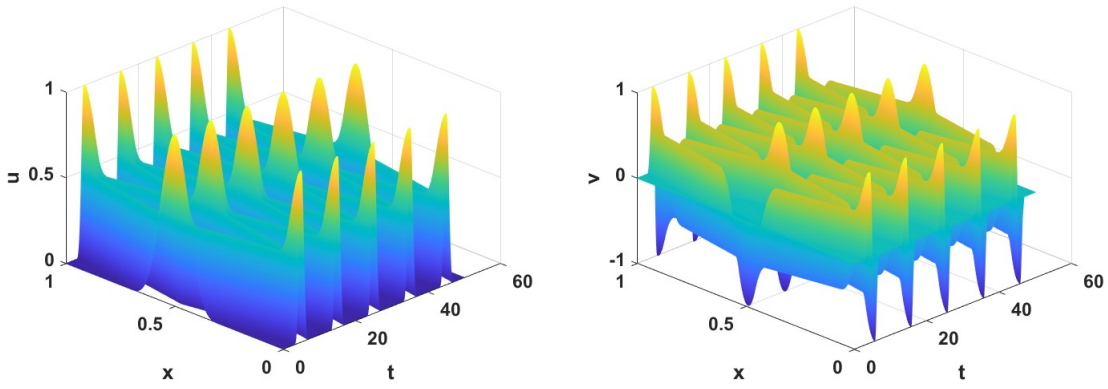

Figure 2.1 Full order model simulation: time evolution of u and v

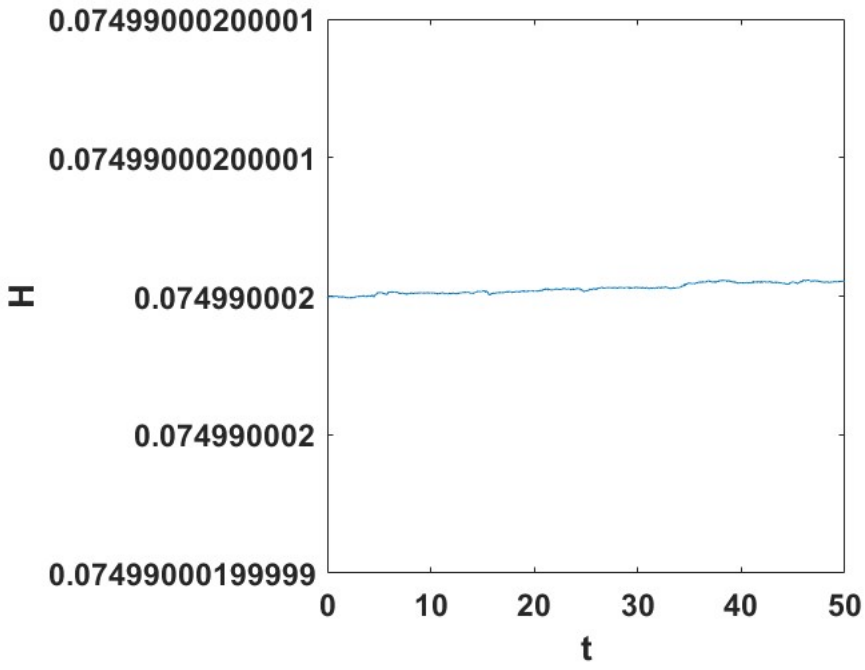

Figure 2.2 A well preserved Hamiltonian generated by the full order model simulation

For calculating the temporal errors, the reference time step size is chosen to be $dt = 0.00125$. The results are listed in Table 2.1. It is seen that the error decays superlinearly, which adequately aligns with the literature cited in Section 2.1

For the spatial errors, the reference mesh is associated with the number of grids,

chosen to be $N = 1024$, while Δt was held constant at 0.001. The results are listed in Table 2.2.

Table 2.1 Full Order Model Error in Time

Δt	0.16	0.08	0.04	0.02	0.01
Error	0.8046	0.2935	0.1038	0.0305	0.0107
Rate		2.7411	2.8289	3.3976	2.8566

Table 2.2 Full Order Model Error in Space

N	32	64	128	256
Error	0.9144	0.5108	0.1953	0.0887
Rate		1.7899	2.6152	2.2022

Chapter 3

Reduced Order Model

3.1 POD Reduced Order Modeling

To create a projection-based model, one must project the governing equations onto a low-dimensional subspace spanned by a POD basis. An in-depth discussion on this process can be found in [7]. Next, we will give a brief discussion on the generation of reduced-order methods for non-parametric systems. For simplicity, we consider the linear system of the following form:

$$\mathbf{E}\dot{\mathbf{x}}(t) = \mathbf{A}\mathbf{x}(t). \tag{3.1}$$

It is important to note that the POD can be applied to nonlinear systems as well. Given the coefficient matrices $\mathbf{E}$ and $\mathbf{A}$, and assuming suitably defined r-dimensional test and trial subspaces with $r << N$, the governing equations are projected onto the low-dimensional subspace. Denote the trial and test basis matrices by $\mathbf{\Phi}$, $\mathbf{W} \in \mathbb{R}^{N\times r}$. Using the approximation $\mathbf{x}(t) \approx \mathbf{\Phi}\mathbf{a}(t)$, where $\mathbf{a}(t) \in \mathbb{R}^r$ and implementing this approximation in (3.1) defines the residual as $\mathbf{E}\mathbf{\Phi}\dot{\mathbf{a}}(t) - \mathbf{A}\mathbf{\Phi}\mathbf{a}(t)$. Utilizing the Petrov-Galerkin yields

$$\mathbf{W}^\top(\mathbf{E}\mathbf{\Phi}\dot{\mathbf{a}}(t) - \mathbf{A}\mathbf{\Phi}\mathbf{a}(t)) = 0. \tag{3.2}$$

This gives the reduced system as

$$\mathbf{E}_r\dot{\mathbf{a}}(t) = \mathbf{A}_r\mathbf{a}(t), \tag{3.3}$$

where $\mathbf{E}_r = \mathbf{W}^\top\mathbf{E}\mathbf{\Phi}$, and $\mathbf{A}_r = \mathbf{W}^\top\mathbf{A}\mathbf{\Phi}$. Visually, the process of projection-based model reduction can be shown in the figure where a large-scale full order model is

compressed to a smaller scale reduced order model. Moreover, when $\mathbf{W}$ is chosen to be $\mathbf{\Phi}$, the projection is Galerkin.

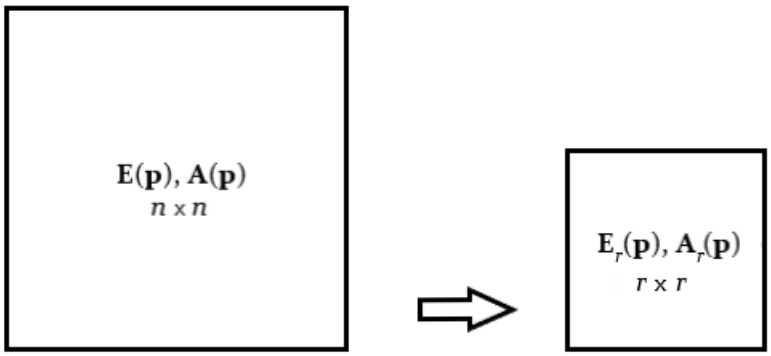

Figure 3.1 Visual representation of reduced order model

The basis matrices, $\mathbf{\Phi}$ and $\mathbf{W}$ can be computed in several ways such as rational interpolation or balanced truncation, as illustrated in [7]. In this paper, we will be focusing on the (time-domain) proper orthogonal decomposition (POD) method. It is important to note that the POD can also be derived in the frequency domain. For more discussion, the reader is referred to [7].

Time Domain POD

Lumley first introduced proper orthogonal decomposition for the analysis of turbulent flows [37]. This method is closely related to methods used in other fields. For example, Karhunen-Loeve expansions were used in stochastic process modeling in [32, 36] as well as empirical orthogonal eigenfunctions used in meteorological modeling [42]. Similar methods have been implemented to study principal component analysis in statistics [30, 26].

In the POD method, the original state variable is approximated by only a few of the dominant global basis functions. Suppose that after numerical discretization, the system has N degrees of freedom in space. If we let $\mathbf{x}_i$ represent numerical

solution at time t_i, then we have that the snapshot data, $\mathbf{X}$, consists of numerical solutions at discrete time steps $t_1, \ldots, t_{N_s}$. In other words, we have the snapshot matrix $\mathbf{X} = [\mathbf{x}_1, \ldots, \mathbf{x}_{N_s}] \in \mathbb{R}^{n \times N_s}$. The POD method sets out to find an orthonormal basis $\Phi = \{\phi_1, \ldots, \phi_r\}$, from the optimization problem given as

$$\min_{\text{Rank}(\Phi)=r} \sum_{j=1}^{M} ||\mathbf{x}_j - \mathbf{\Phi}\mathbf{\Phi}^\top \mathbf{x}_j||^2. \tag{3.4}$$

We note here that $\mathbf{\Phi}^\top \mathbf{\Phi} = I_r$, which is the $r \times r$ identity matrix, and $||\cdot||$ denotes the 2-norm. The POD basis vectors, $\phi_1, \ldots, \phi_r$, are the left singular vectors of $\mathbf{X}$ that correspond to the first r nonzero singular values $\sigma_1 \geq \sigma_2 \geq \cdots \geq \sigma_r > 0$. When $\mathbf{X}$ has dimensions $N << N_s$, the POD basis can be found by applying the method of singular value decomposition (SVD). However, when $\mathbf{X}$ has dimensions $N >> N_s$, the method of snapshots can be applied instead. For a discussion of an approximate method of snapshots and its effectiveness at further reducing computational complexity, the reader is directed to [56].

In an ideal scenario, the entire continuous trajectory of the system is assumed to be available on the whole time interval $[0, T]$. For this case, we can take the trajectory, $\mathbf{x}(t)$ to be the snapshot, and use the POD method to find the set of optimal basis functions $\{\phi_1, \ldots \phi_r\}$ by minimizing the projection error of $\mathbf{x}(t)$ onto the subspace spanned by the basis, i.e.

$$\min_{\text{Rank}(\Phi)=r} \int_0^T ||\mathbf{x}_j - \mathbf{\Phi}\mathbf{\Phi}^\top \mathbf{x}_j||^2 dt. \tag{3.5}$$

The solution to this optimization problem is equivalent to finding the first r dominant eigenvectors of the snapshot covariant matrix $\mathbf{R} = \int_0^T \mathbf{x}(t)\mathbf{x}(t)^\top dt$ [22].

The framework of the POD reduced order modeling is summarized in Algorithm 1. We emphasize the approach can be applied to nonlinear systems as well, although the linear system (3.1) is discussed here.

Algorithm 1 POD-G-ROM Generation

Given $\mathbf{x}(t)$ resulting from the system (3.1) for $t \in (t_0, t_0 + T)$

1. Compute POD basis vectors

$$\{\phi_1, \phi_2, \ldots, \phi_r\}$$

from snapshots and construct the basis matrix

$$\mathbf{\Phi} = [\phi_1, \phi_2, \ldots, \phi_r].$$

Assume the reduced-order approximation

$$\mathbf{x}_r(t) \approx \sum_{j=1}^{r} \phi_j a_j(t) \in \text{span}\{\phi_1, \phi_2, \ldots, \phi_r\}, \tag{3.6}$$

where $\{\mathbf{a}_j(t)\}_{j=1}^r$ are the time-varying POD basis coefficient functions.

2. Substitute the POD approximation into the full-order system and then apply the Galerkin procedure.

$$\left\langle \sum_{j=1}^{r} \mathbf{E}\phi_j \dot{a}_j(t), \phi_i \right\rangle = \left\langle \mathbf{A} \sum_{j=1}^{r} \phi_j \dot{a}_j(t), \phi_i \right\rangle,$$

$$\left\langle \sum_{j=1}^{r} \phi_j \dot{a}_j(0), \phi_i \right\rangle = \left\langle x_0, \phi_i \right\rangle \text{ for } i = 1, \ldots, r,$$

which gives the POD-G-ROM for $\{\mathbf{a}_j(t)\}_{j=1}^r$:

$$\mathbf{E}\dot{a}_i(t) = \left\langle \mathbf{A} \sum_{j=1}^{r} \phi_j a_j(t), \phi_i \right\rangle, \tag{3.7}$$

with

$$a_i(0) = \left\langle x_0, \phi_i \right\rangle \text{ for } i = 1, \ldots, r.$$

3.2 POD-ROM for Hamiltonian Systems

Adapting the POD-ROM for Hamiltonian systems introduces the need to retain the appropriate geometric structure. In fact, after a spatial discretization of the general Hamiltonian PDE (2.1), the finite dimensional Hamiltonian ODE system is given by

$$\dot{\mathbf{u}} = \mathbf{D}\nabla_{\mathbf{u}} H(\mathbf{u}), \tag{3.8}$$

where $\mathbf{D}$ is a skew-symmetric matrix. This system is accompanied by te initial condition $\mathbf{u}(t_0) = \mathbf{u}_0$. Suppose that the POD basis matrix, $\mathbf{\Phi}$, is found and the approximation of the state variable $\mathbf{u}$ is represented by $\mathbf{u}_r = \mathbf{\Phi}\mathbf{a}(t)$, where $\mathbf{a}(t)$ is the unknown coefficient vector. If we substitute $\mathbf{u}$ with $\mathbf{u}_r$ in (3.8), we obtain

$$\Phi\dot{\mathbf{a}} = \mathbf{D}\nabla_{\mathbf{u}} H(\mathbf{\Phi}\mathbf{a}). \tag{3.9}$$

We then implement the Galerkin method by multiplying $\mathbf{\Phi}^\top$ to each side of the equation, which yields

$$\dot{\mathbf{a}} = \mathbf{\Phi}^\top\mathbf{D}\nabla_{\mathbf{u}} H(\mathbf{\Phi}\mathbf{a}). \tag{3.10}$$

The time derivative of the Hamiltonian function $H(\mathbf{\Phi}\mathbf{a})$, which represents the energy of the system, is then given by

$$\begin{aligned}
\frac{d}{dt}H(\mathbf{\Phi}\mathbf{a}) &= [\nabla_{\mathbf{a}} H(\mathbf{\Phi}\mathbf{a})^\top\dot{\mathbf{a}}] \\
&= [\mathbf{\Phi}^\top\nabla_{\mathbf{u}} H(\mathbf{\Phi}\mathbf{a})]^\top\mathbf{\Phi}^\top\mathbf{D}\nabla_{\mathbf{u}} H(\mathbf{\Phi}\mathbf{a}) \\
&= \nabla_{\mathbf{u}} H(\mathbf{\Phi}\mathbf{a})^\top\mathbf{\Phi}\mathbf{\Phi}^\top\mathbf{D}\nabla_{\mathbf{u}} H(\mathbf{\Phi}\mathbf{a}).
\end{aligned}$$

In the previous equation, the fact that $\nabla_{\mathbf{a}} H(\mathbf{\Phi}\mathbf{a}) = \mathbf{\Phi}^\top\nabla_{\mathbf{u}} H(\mathbf{\Phi}\mathbf{a})$ was used. We recall that $\mathbf{\Phi}$ is composed of the dominant r left singular vectors of the snapshot matrix. This gives us two cases for the dimensions of the matrix. For the first case,

when $r = n$, we have that $\mathbf{\Phi}$ is a square unitary matrix. This gives us $\mathbf{\Phi}\mathbf{\Phi}^\top = I_n$ and $\frac{d}{dt}H(\mathbf{\Phi a}) = 0$, since $\mathbf{D}$ is skew-symmetric. This tells us that the Hamiltonian is a constant. However, in the case when $r << n$, $\mathbf{\Phi}$ is no longer a square matrix and therefore $\mathbf{\Phi}\mathbf{\Phi}^\top\mathbf{D}$ is not skew-symmetric. This no longer guarantees that the Hamiltonian function is preserved. Next, we consider the wave equation and test the performance of the Galerkin projection-based POD-ROM.

3.3 Numerical Experiments

Consider the same wave equation, (2.10), with $g = 0$, discussed in the previous chapter. Based on the snapshots from the full order simulation, following the method outlined in Algorithm 1, we obtain the POD-ROM.

To complete this snapshot simulation, data snapshots are collected from the FOM at intervals of 50 time steps. Then the SVD is used to find the $r-$dimensional POD basis $\mathbf{\Phi}_u$ and $\mathbf{\Phi}_v$. Then, we obtain the POD approximations given by

$$\mathbf{u}_r(t) = \mathbf{\Phi}_u\mathbf{a}(t) \qquad \mathbf{v}_r(t) = \mathbf{\Phi}_v\mathbf{b}(t). \tag{3.11}$$

The POD-ROM is then generated by substituting the approximations into the FOM before applying the Galerkin projection. This model reads

$$\begin{bmatrix} \dot{\mathbf{a}} \\ \dot{\mathbf{b}} \end{bmatrix} = \begin{bmatrix} \mathbf{\Phi}_u^\top\mathbf{\Phi}_v\mathbf{b} \\ \mathbf{\Phi}_v^\top\mathbf{A}\mathbf{\Phi}_u\mathbf{a} \end{bmatrix} \tag{3.12}$$

Using the implicit midpoint rule, which is equivalent to the AVF method in the linear case, the method satisfies

$$\begin{bmatrix} \frac{\mathbf{a}^{k+1}-\mathbf{a}^k}{\Delta t} \\ \frac{\mathbf{b}^{k+1}-\mathbf{b}^k}{\Delta t} \end{bmatrix} = \begin{bmatrix} \mathbf{\Phi}_u^\top\mathbf{\Phi}_v\frac{\mathbf{b}^{k+1}-\mathbf{b}^k}{2} \\ \mathbf{\Phi}_v^\top\mathbf{A}\mathbf{\Phi}_u\frac{\mathbf{a}^{k+1}-\mathbf{a}^k}{2} \end{bmatrix} \tag{3.13}$$

with $\mathbf{a}^0 = \mathbf{\Phi}_u^\top\mathbf{u}_0$ and $\mathbf{b}^0 = \mathbf{\Phi}_v^\top\mathbf{v}_0$.

It is observed that the maximum error of $\varepsilon_\infty = 0.4591$ is obtained for$r = 5$, with a CPU time of 0.069912 seconds; while the maximum error for $r = 20$ is significantly smaller than that obtained for $r = 5$, at $\varepsilon_\infty = 0.02079$. The CPU time for $r = 20$ is found to be 0.10622. The numerical errors in the Hamiltonian function values and the state vectors are shown in Figures 3.2, 3.3 and 3.4.

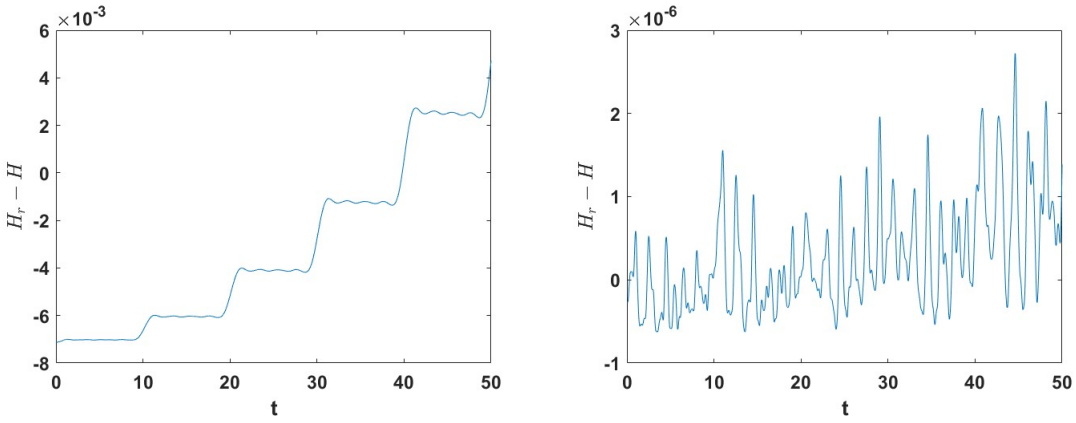

Figure 3.2 Linear wave reduced order model Hamiltonian error results for $r = 5$ (left) and $r = 20$ (right)

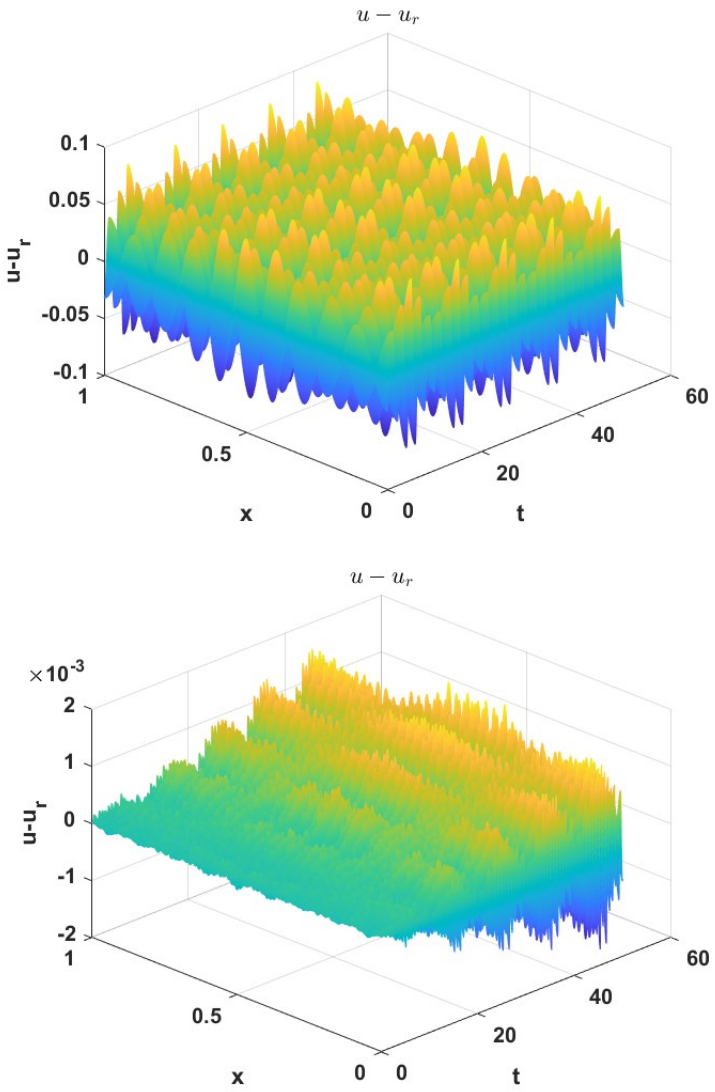

Figure 3.3 Linear wave reduced order model u error for $r = 5$ (top) and $r = 20$ (bottom)

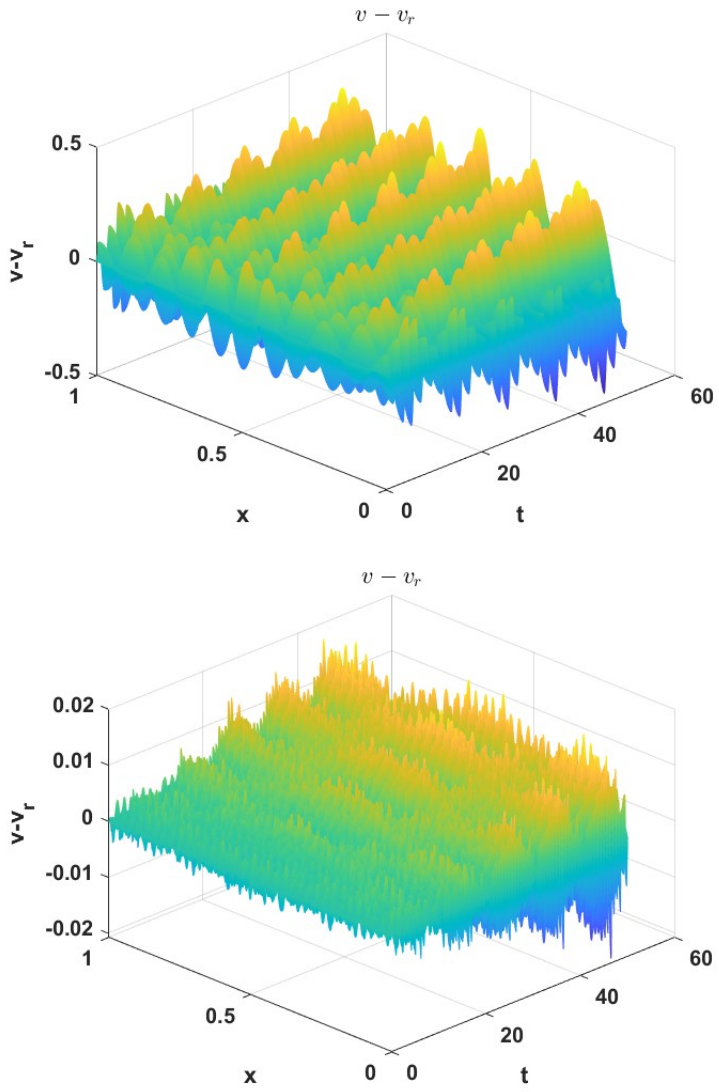

Figure 3.4 Linear wave reduced order model v error for $r = 5$ (top) and $r = 20$ (bottom)

Chapter 4

Structure Preserving Reduced Order Model

4.1 SP-ROM for Hamiltonian Systems

In order to keep the geometric structure of the Hamiltonian system, Gong et al,, in [22], assume that there exists a matrix $\mathbf{D}_r$ such that

$$\mathbf{\Phi}^\top \mathbf{D} = \mathbf{D}_r \mathbf{\Phi}^\top. \tag{4.1}$$

With this new $\mathbf{D}_r$, the Galerkin projection-based ROM can now be written as

$$\begin{aligned}\dot{\mathbf{a}} &= \mathbf{\Phi}^\top \mathbf{D} \nabla_{\mathbf{u}} H(\mathbf{\Phi a}) \\ &= \mathbf{D}_r \mathbf{\Phi}^\top \nabla_{\mathbf{u}} H(\mathbf{\Phi a}) \\ &= \mathbf{D}_r \nabla_{\mathbf{a}} H(\mathbf{\Phi a})\end{aligned}$$

with an initial condition of $\mathbf{a}(t_0) = \mathbf{\Phi}^\top \mathbf{u}_0$. In this new reduced-order system, the time derivative of the Hamiltonian function can be written as

$$\begin{aligned}\frac{d}{dt} H(\mathbf{\Phi a}) &= [\nabla_{\mathbf{a}} H(\mathbf{\Phi a})^\top \dot{\mathbf{a}}] \\ &= [\nabla_{\mathbf{a}} H(\mathbf{\Phi a})]^\top \mathbf{D}_r \nabla_{\mathbf{a}} H(\mathbf{\Phi a}) \\ &= 0, \qquad \text{if } \mathbf{D}_r \text{ is skew-symmetric.}\end{aligned}$$

By right multiplying both sides of (4.1) by $\mathbf{\Phi}$, we have the normal equation solution given by

$$\mathbf{D}_r = \mathbf{\Phi}^\top \mathbf{D} \mathbf{\Phi}. \tag{4.2}$$

This yields the structure preserving ROM (SP-ROM):

$$\dot{\mathbf{a}} = \mathbf{D}_r \nabla_a H(\mathbf{\Phi a}), \tag{4.3}$$

where $\mathbf{D}_r$ is skew-symmetric.

4.2 Numerical Experiments

In this subsection, we still consider the wave equation and investigate the performance of SP-ROMs generated using different POD basis. In particular, SP-ROM-0 uses the standard POD basis, SP-ROM-1 uses the enriched POD basis, and SP-ROM-2 uses the shifted POD basis.

4.2.1 SP-ROM based on the standard POD basis

First consider a new structure-preserving ROM using a standard POD basis denoted by SP-ROM-0, that reads:

$$\begin{bmatrix} \dot{\mathbf{a}} \\ \dot{\mathbf{b}} \end{bmatrix} = \begin{bmatrix} 0 & \mathbf{\Phi}_u^\top \mathbf{\Phi}_v \\ -\mathbf{\Phi}_v^\top \mathbf{\Phi}_u & 0 \end{bmatrix} \begin{bmatrix} -\mathbf{\Phi}_u^\top \mathbf{A} \mathbf{\Phi}_\mathbf{u} \mathbf{a} \\ \mathbf{b} \end{bmatrix} \tag{4.4}$$

We note that the new ROM has the same structure as that of the FOM, namely, the coefficient matrix is skew-symmetric. We expect a constant Hamiltonian function approximation by the AVF method given the SP-ROM would become a canonical Hamiltonian system when $\mathbf{\Phi}_v = \mathbf{\Phi}_u$. After discretization, the model (4.4) now reads as:

$$\begin{bmatrix} \frac{\mathbf{a}^{k+1}-\mathbf{a}^k}{\Delta t} \\ \frac{\mathbf{b}^{k+1}-\mathbf{b}^k}{\Delta t} \end{bmatrix} = \begin{bmatrix} 0 & \mathbf{\Phi}_u^\top \mathbf{\Phi}_v \\ -\mathbf{\Phi}_v^\top \mathbf{\Phi}_u & 0 \end{bmatrix} \begin{bmatrix} -\mathbf{\Phi}_u^\top \mathbf{A} \mathbf{\Phi}_u \frac{\mathbf{a}^{k+1}+\mathbf{a}^k}{2} \\ \frac{\mathbf{b}^{k+1}+\mathbf{b}^k}{2} \end{bmatrix}. \tag{4.5}$$

When we choose $r = 5$, the maximum error is found to be $\varepsilon_\infty = 0.26062$ and the CPU time is 0.073753 seconds. This error decreases significantly to $\varepsilon_\infty = 0.0058203$ when $r = 20$ and the CPU time is 0.061384 seconds. A comparison of the Hamiltonian errors is shown in Figure 4.1, while the errors for u and v are shown in Figures 4.2 and 4.3, respectively. It is seen that when $r = 5$, the difference between H_r and H is on the order of 10^{-3}.

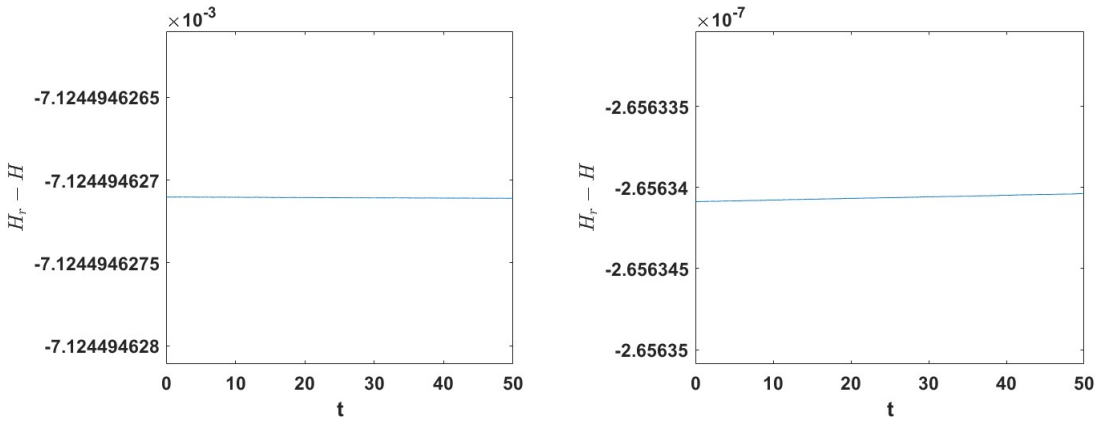

Figure 4.1 SP-ROM-0: Hamiltonian error plots for $r = 5$ (left) and $r = 20$ (right).

4.2.2 SP-ROM based on enriched POD basis

We now focus on the POD basis with a corrected Hamiltonian feature. This additional basis function is calculated from the residual of approximating the initial data. After normalization, the enriched POD basis becomes $\tilde{\mathbf{\Phi}}_u = [\mathbf{\Phi}_u, \psi_u]$ and $\tilde{\mathbf{\Phi}}_v = [\mathbf{\Phi}_v, \psi_v]$. The new variation of the SP-ROM with the enriched POD basis is denoted by SP-ROM-1, which reads

$$\begin{bmatrix} \dot{\mathbf{a}} \\ \dot{\mathbf{b}} \end{bmatrix} = \begin{bmatrix} 0 & \tilde{\mathbf{\Phi}}_u^\top \tilde{\mathbf{\Phi}}_v \\ -\tilde{\mathbf{\Phi}}_v^\top \tilde{\mathbf{\Phi}}_u & 0 \end{bmatrix} \begin{bmatrix} -\tilde{\mathbf{\Phi}}_u^\top \mathbf{A} \tilde{\mathbf{\Phi}}_u \mathbf{a} \\ \mathbf{b} \end{bmatrix}, \tag{4.6}$$

with the discretized version of the system given by

$$\begin{bmatrix} \frac{\mathbf{a}^{k+1}-\mathbf{a}^k}{\Delta t} \\ \frac{\mathbf{b}^{k+1}-\mathbf{b}^k}{\Delta t} \end{bmatrix} = \begin{bmatrix} 0 & \tilde{\mathbf{\Phi}}_u^\top \tilde{\mathbf{\Phi}}_v \\ -\tilde{\mathbf{\Phi}}_v^\top \tilde{\mathbf{\Phi}}_u & 0 \end{bmatrix} \begin{bmatrix} -\tilde{\mathbf{\Phi}}_u^\top \mathbf{A} \tilde{\mathbf{\Phi}}_u \frac{\mathbf{a}^{k+1}+\mathbf{a}^k}{2} \\ \frac{\mathbf{b}^{k+1}+\mathbf{b}^k}{2} \end{bmatrix}. \tag{4.7}$$

The goal of the SP-ROM-1 is to improve the accuracy after introducing the extra basis function. It is observed that the difference between H_r and H reduced to 10^{-12} when $r = 5$ and to 10^{-13} when $r = 20$. Meanwhile, the max error is found to increase to $\varepsilon_\infty = 0.41378$ and the CPU time is 0.038486 seconds. For $r = 20$, the max error

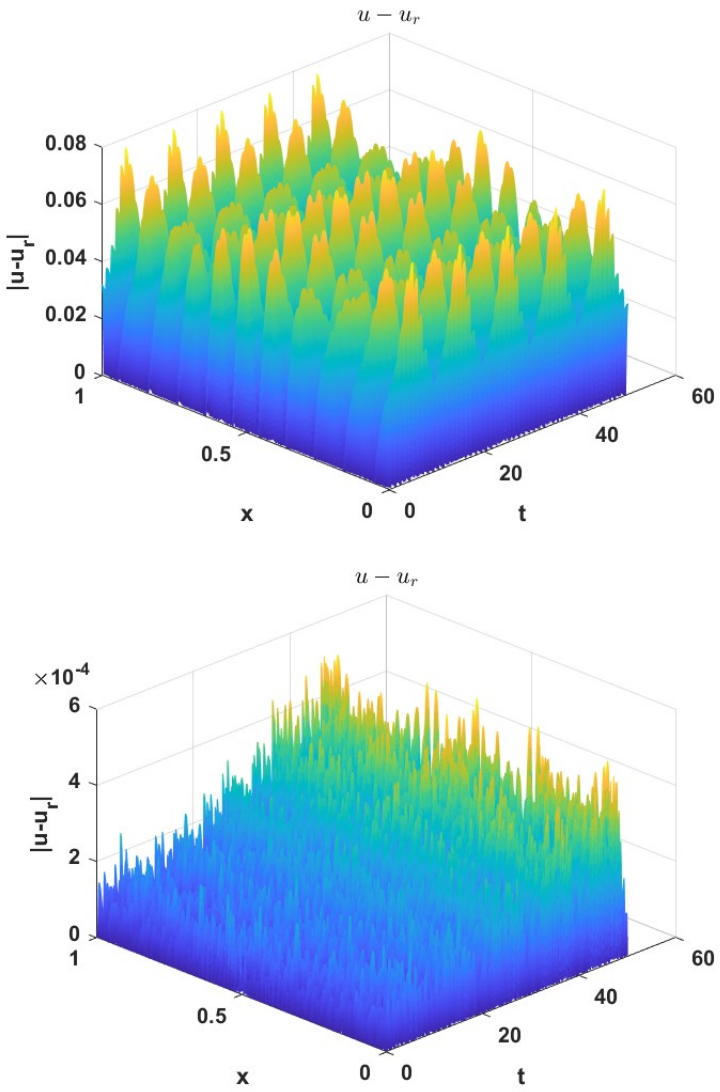

Figure 4.2 SP-ROM-0: u error plots for $r = 5$ (top) and $r = 20$ (bottom).

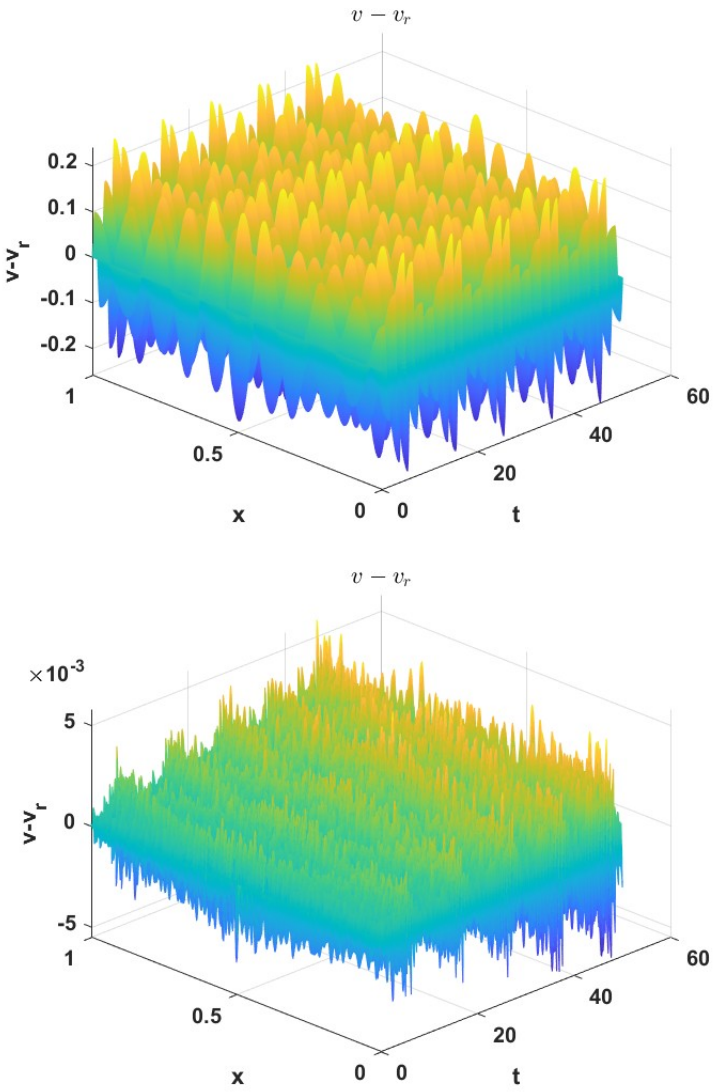

Figure 4.3 SP-ROM-0: v error plots for $r = 5$ (top) and $r = 20$ (bottom).

is once again found to be higher than that of SP-ROM-0, at $\varepsilon_\infty = 0.0083028$ and the CPU time is 0.059882 seconds.

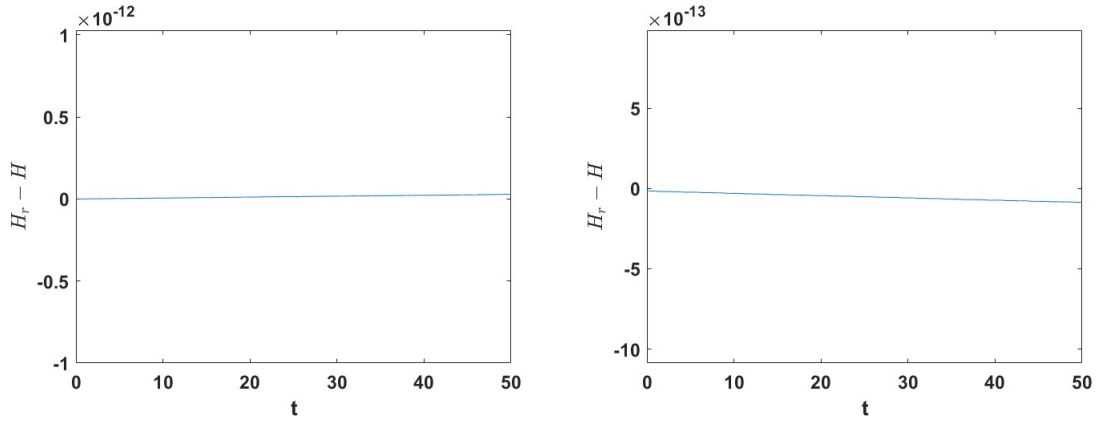

Figure 4.4 SP-ROM-1: Hamiltonian error plots for $r = 5$ (left) and $r = 20$ (right).

4.2.3 SP-ROM based on shifted POD basis

For a third approach, a POD basis of shifted snapshots is employed in the structure-preserving ROM. This model attempts to correct the Hamiltonian approximation error caused by the information lost through the POD truncation. The new model, denoted by SP-ROM-2 reads

$$\begin{bmatrix} \dot{\mathbf{a}} \\ \dot{\mathbf{b}} \end{bmatrix} = \begin{bmatrix} 0 & \boldsymbol{\Phi}_u^\top \boldsymbol{\Phi}_v \\ -\boldsymbol{\Phi}_v^\top \boldsymbol{\Phi}_u & 0 \end{bmatrix} \left(\begin{bmatrix} -\boldsymbol{\Phi}_u^\top \mathbf{A} \boldsymbol{\Phi}_u \mathbf{a} \\ \mathbf{b} \end{bmatrix} + \begin{bmatrix} -\boldsymbol{\Phi}_u^\top \mathbf{A} \mathbf{u}_0 \\ \boldsymbol{\Phi}_v^\top \mathbf{v}_0 \end{bmatrix} \right). \tag{4.8}$$

Following the same AVF method, we obtain the discrete system,

$$\begin{bmatrix} \frac{\mathbf{a}^{k+1} - \mathbf{a}^k}{\Delta t} \\ \frac{\mathbf{b}^{k+1} - \mathbf{b}^k}{\Delta t} \end{bmatrix} = \begin{bmatrix} 0 & \boldsymbol{\Phi}_u^\top \boldsymbol{\Phi}_v \\ -\boldsymbol{\Phi}_v^\top \boldsymbol{\Phi}_u & 0 \end{bmatrix} \left(\begin{bmatrix} -\boldsymbol{\Phi}_u^\top \mathbf{A} \boldsymbol{\Phi}_u \frac{\mathbf{a}^{k+1} + \mathbf{a}^k}{2} \\ \frac{\mathbf{b}^{k+1} + \mathbf{b}^k}{2} \end{bmatrix} + \begin{bmatrix} -\boldsymbol{\Phi}_u^\top \mathbf{A} \mathbf{u}_0 \\ \boldsymbol{\Phi}_v^\top \mathbf{v}_0 \end{bmatrix} \right), \tag{4.9}$$

with the choice of $\mathbf{a}^0 = \mathbf{0}$ and $\mathbf{b}^0 = \mathbf{0}$.

Figure 4.7 shows the time evolution of the Hamiltonian function errors. It is seen that the difference between H_r and H is on the order of 10^{-14} for both $r = 5$ and $r = 20$. Figures 4.8 and 4.9 present the errors for approximating u and v, respectively.

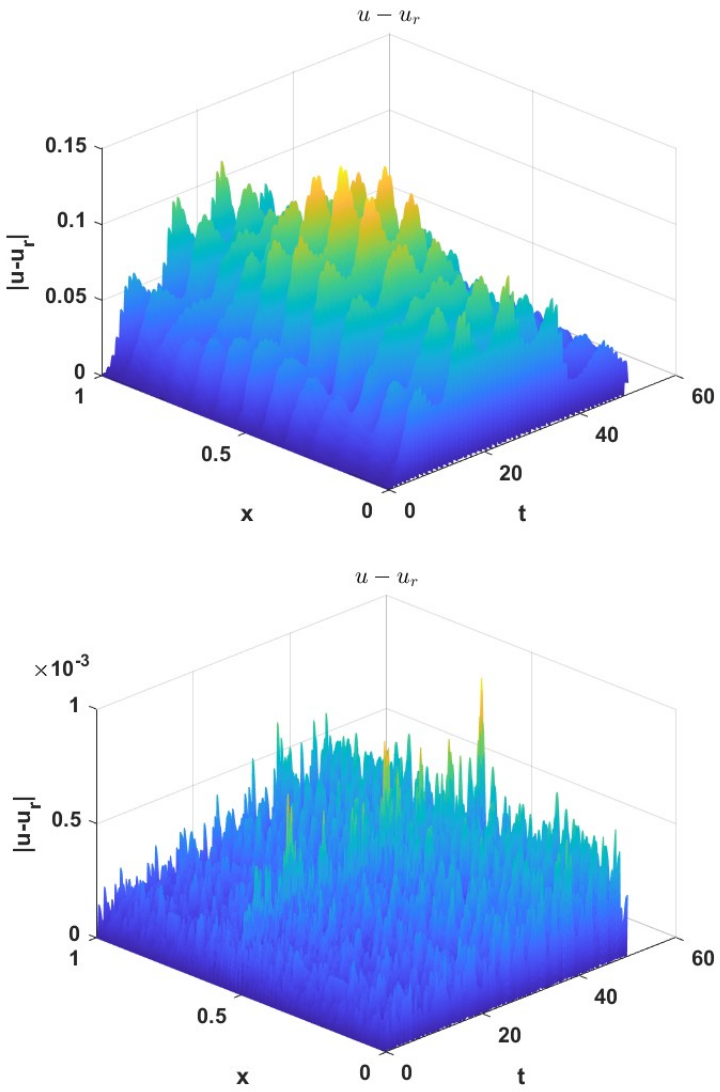

Figure 4.5 SP-ROM-1: u error plots for $r = 5$ (top) and $r = 20$ (bottom).

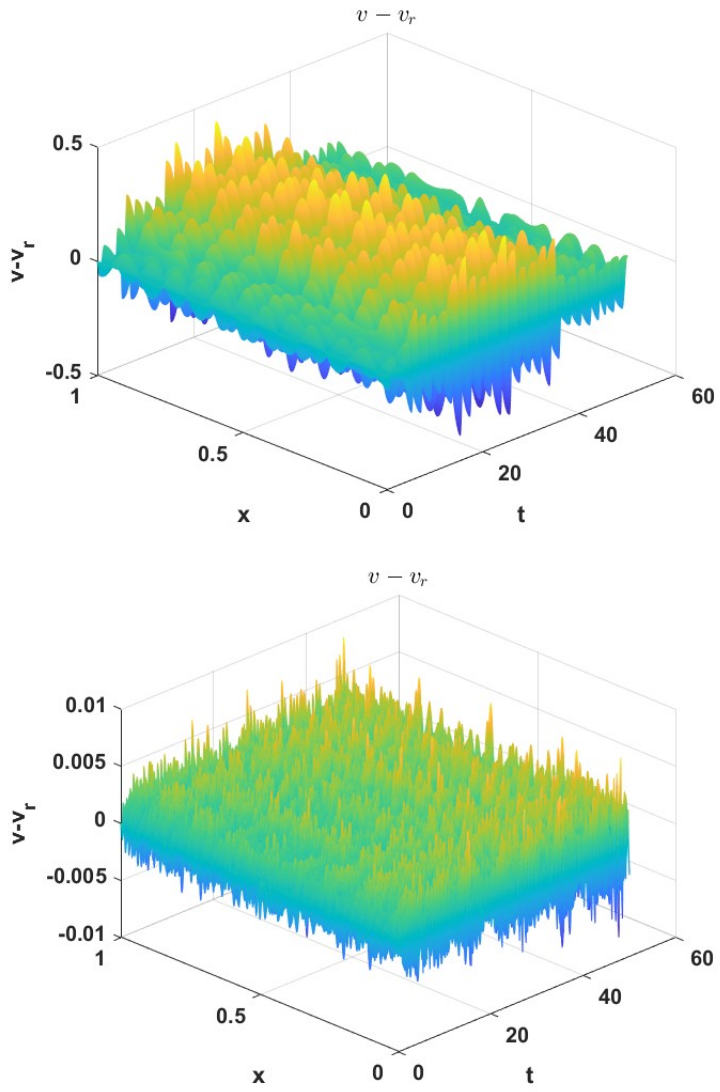

Figure 4.6 SP-ROM-1: v error plots for $r = 5$ (top) and $r = 20$ (bottom).

The maximum error for the $r = 5$ model is found to be $\varepsilon_\infty = 0.15257$ and the CPU time is 0.10815 seconds. For $r = 20$, the max error is $\varepsilon_\infty = 0.016747$ while the CPU time is 0.15899 seconds.

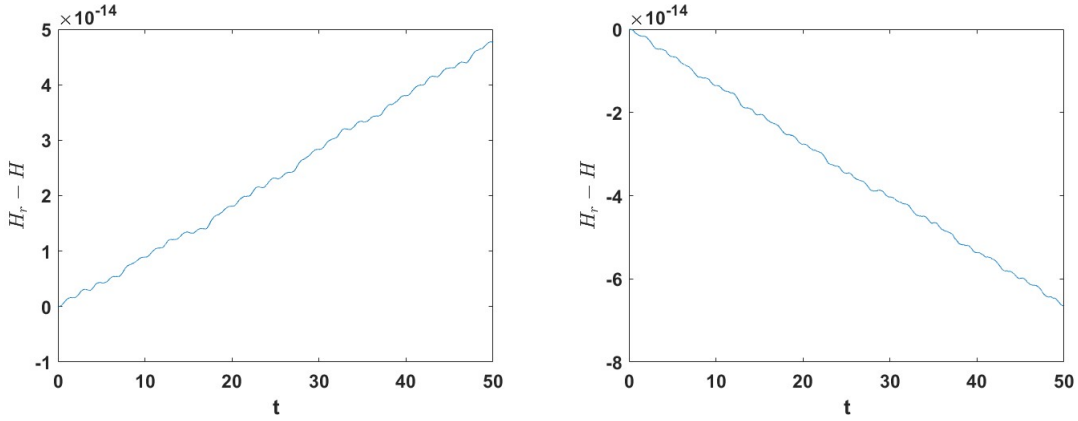

Figure 4.7 SP-ROM-2: Hamiltonian error plots for $r = 5$ (left) and $r = 20$ (right).

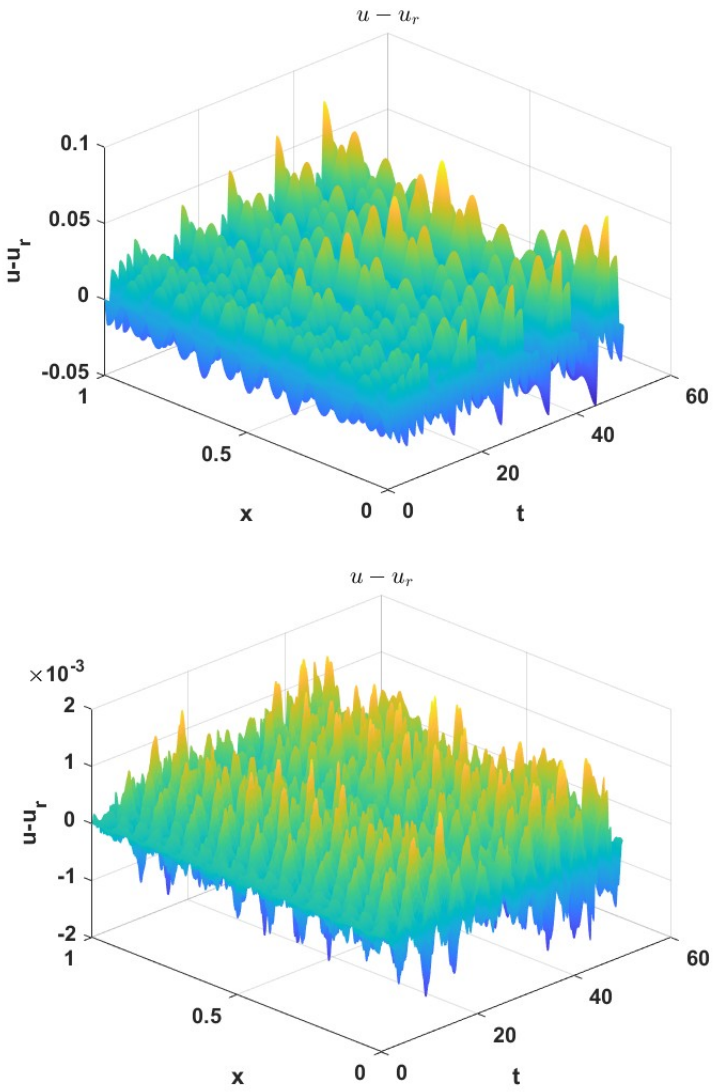

Figure 4.8 SP-ROM-2: u error plots for $r = 5$ (top) and $r = 20$ (bottom).

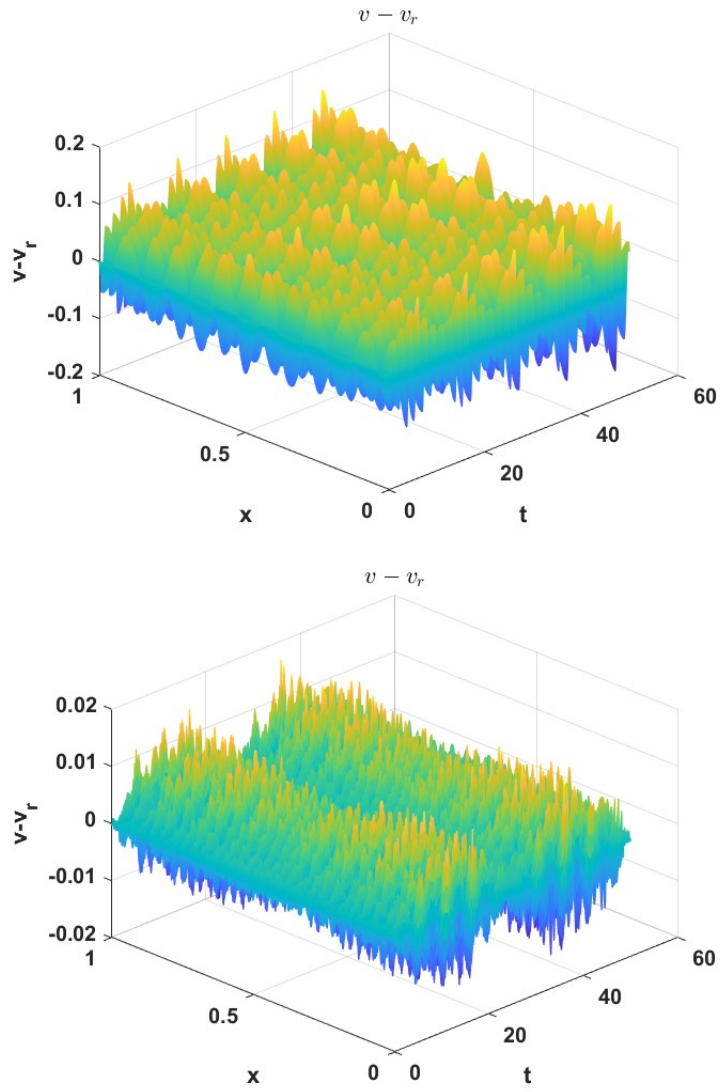

Figure 4.9 SP-ROM-2: v error plots for $r = 5$ (top) and $r = 20$ (bottom).

Chapter 5

Structure Preserving Nonlinear Reduced Order Model

5.1 SP-DEIM for Hamiltonian Systems

So far, the discussion has been limited to the linear system. When a nonlinear model is considered, the computational complexity of the POD-ROM could still depend on the number of degrees of freedom of the FOM. To overcome this issue, the discrete empirical interpolation method (DIEM) for model reduction is introduced [15].

In general, when the DIEM is used to approximate a nonlinear function $\mathbf{f}(\mathbf{u}(t))$, by

$$\mathbf{f}(\mathbf{u}(t)) \approx \sum_{j=1}^{s} \psi_j c_j(t), \tag{5.1}$$

where ψ_j is the j-th DEIM basis vector generated from the nonlinear snapshots

$$[\mathbf{f}(\mathbf{u}(t_1)), \mathbf{f}(\mathbf{u}(t_2)), \ldots, \mathbf{f}(\mathbf{u}(t_m))] .$$

For convenience, this algorithm is detailed in Algorithm 2, by which the method selects a set of interpolation points $\wp := [e_{\wp_1}, \ldots, e_{\wp_s}]^\top$ and c_{p_i} is the $\wp_i$-th column of the identity matrix. As a result, the DEIM approximates the nonlinear function by

$$\mathbf{f}(\mathbf{u}) \approx \mathbf{\Psi}(\mathbf{P}^\top \mathbf{\Psi})^{-\mathbf{1}} \mathbf{P}^\top \mathbf{f}(\mathbf{u}), \tag{5.2}$$

where $\mathbf{P} = [e_{\wp_1}, \ldots, e_{\wp_a}] \in \mathbb{R}^{N \times N}$ and $\mathbf{\Psi} = [\psi_1, \ldots, \psi_s] \in \mathbb{R}^{N \times s}$ is the DEIM basis matrix. This algorithm reduces the online computation since $\mathbf{f}$ is only being evaluated

Algorithm 2 DEIM

input: $\{\psi_\ell\}_{\ell=1}^{s} \subset \mathbb{R}^s$ linear independent
Output: $\wp = [\wp_1, \ldots, \wp_s]^\top \in \mathbb{R}^s$
$[|\rho|, \wp_1] = \max\{|\psi_1|\}$;
$\Psi = [\psi_1], \mathbf{P} = [e_{\wp_1}, \wp = [\wp_1]$;
for $\ell = 2$ **to** s **do**
Solve $(\mathbf{P}^\top \mathbf{\Psi})\mathbf{c} = \mathbf{P}^\top \psi_\ell$ for $\mathbf{c}$;
$\mathbf{r}$=$\psi_\ell - \mathbf{\Psi c}$; $[|\rho|, \wp_\ell] = \max\{|r|\}$;
$\mathbf{\Psi} \longleftarrow [\Psi \quad \psi_\ell], \mathbf{P} \longleftarrow [P \quad \mathbf{e}_{\wp_\ell}], \wp \longleftarrow \begin{bmatrix} \wp \\ \wp_\ell \end{bmatrix}$;

at s number of points. An in-depth analysis of the method is conducted in [15].

As for the Hamiltonian system, when D depends nonlinearly on $\mathbf{u}$, the computational complexity depends on the number of degrees of freedom in the FOM. Thus, the DIEM is combined with the tensor product and vectorization to reduce the complexity [40]. A more difficult case is when the gradient of Hamiltonian inherits a non-polynomial nonlinearity, the computational cost could also depend on N. In [14], Chaturantabut et al. suggest a DEIM hamiltonian where $H(\mathbf{u})$ is split into two parts:

$$H(\mathbf{u}) = \frac{1}{2}\mathbf{u}^\top \mathbf{Q}\mathbf{u} + h(\mathbf{u}). \tag{5.3}$$

After incorporating the DEIM projection of its gradient, $\mathbb{P} = \mathbf{\Psi}(\mathbf{P}^\top \mathbf{\Psi})^{-\mathbf{1}}\mathbf{P}^\top$, $h(\mathbf{u})$ is approximated by $h(\mathbb{P}^\top \mathbf{u})$. These could lead to some errors due to the fact that $\mathbf{u}$ is approximated by $\mathbb{P}^\top \mathbf{u}$, but $\mathbb{P}$ is derived from the DEIM on $\nabla_u h(\mathbf{u})$.

A possible solution is proposed in [31], where $\nabla_u h(\mathbf{u})$ is directly approximated by its DEIM interpolation $\mathbb{P}\nabla_u h(\mathbf{u})$. However, for this approach, there is not an explicit formula for the discrete Hamiltonian, which means the discrete energy cannot be preserved exactly.

Another possible solution to handle this issue involves applying the DEIM to approximate the Hamiltonian function, but not to its gradient, as in [55]. For now, we write the discrete Hamiltonian function as

$$H(\mathbf{u}) = \frac{1}{2}\mathbf{u}^\top \mathbf{Q}\mathbf{u} + \mathbf{c}^\top \mathbf{G}(\mathbf{u}), \tag{5.4}$$

where $\mathbf{G}(\cdot)$ is a nonlinear vector-valued function of $\mathbf{u}$, and $\mathbf{c}^\top \mathbf{G}(\mathbf{u})$ represents the non-polynomial nonlinearity. The following DEIM interpolation for $\mathbf{G}(\mathbf{u})$ is generated after collecting snapshots, $[\mathbf{G}(\mathbf{u}(t_0)), \ldots, \mathbf{G}(\mathbf{u}(t_m))]$, then

$$\mathbf{G}(\mathbf{u}) \approx \mathbb{P}\mathbf{G}(\mathbf{u}) = \mathbf{\Psi}(\mathbf{P}^\top \mathbf{\Psi})^{-1} \mathbf{P}^\top \mathbf{G}(\mathbf{u}). \tag{5.5}$$

The corresponding reduced Hamiltonian is given by

$$H_r(\mathbf{\Phi a}) = \frac{1}{2}\mathbf{a}\mathbf{Q}_r\mathbf{a} + \mathbf{c}^\top \mathbb{P}\mathbf{G}(\mathbf{\Phi a}), \tag{5.6}$$

where $\mathbf{Q}_r = \mathbf{\Phi}^\top \mathbf{Q}\mathbf{\Phi}$. The associated gradient can be expressed as

$$\nabla_{\mathbf{a}} H_r(\mathbf{a}) = \mathbf{Q}_r\mathbf{a} + \Phi^\top \mathbf{J}_{\mathbf{G}}(\mathbf{\Phi a})\mathbb{P}^\top \mathbf{c}. \tag{5.7}$$

Here, the Jacobian matrix of $\mathbf{G}(\mathbf{u})$ is represented as $\mathbf{J}_{\mathbf{G}}(\cdot)$. Finally, the structure preserving DEIM (SP-DEIM) model is created by plugging equation (5.7) into the SP-ROM (4.3), which leads to

$$\dot{\mathbf{a}} = \mathbf{D}_r[\mathbf{Q}_r\mathbf{a} + \mathbf{\Phi}^\top \mathbf{J}_{\mathbf{G}}(\mathbf{\Phi a})\mathbb{P}^\top \mathbf{c}]. \tag{5.8}$$

Next, we investigate two versions of the SP-DEIM ROM applied to a nonlinear wave equation. The first, called the SP-DEIM-1, uses the standard POD and DEIM basis, while the other, the SP-DEIM-2, uses the shifted snapshot POD basis. In both versions, the number of DEIM basis is selected to be twice as many as that of the POD basis.

5.2 Numerical Experiments

Consider a one-dimensional semilinear awve equation with a constant wave speed c and a nonlinear forcing term $g(u)$:

$$u_{tt} = c^2 u_{xx} - g(u), \quad 0 \le x \le l \text{ and } 0 \le t \le T. \tag{5.9}$$

Written in the Hamiltonian formulation, we have

$$\begin{bmatrix} \dot{u} \\ \dot{v} \end{bmatrix} = \begin{bmatrix} 0 & 1 \\ -1 & 0 \end{bmatrix} \begin{bmatrix} \frac{\delta \mathcal{H}}{\delta u} \\ \frac{\delta \mathcal{H}}{\delta v} \end{bmatrix}. \tag{5.10}$$

This system has a constant Hamiltonian given by

$$\mathcal{H}(t) = \int_0^l \Big[\frac{1}{2}v^2 + \frac{c^2}{2}u_x^2 + G(u)\Big]dx, \tag{5.11}$$

in which $G'(u) = g(u)$, $\frac{\delta \mathcal{H}}{\delta u} = -c^2 u_{xx} + g(u)$ and $\frac{\delta \mathcal{H}}{\delta v} = v$. After using the central finite difference method, the system (5.10) now reads

$$\begin{bmatrix} \dot{\mathbf{u}} \\ \dot{\mathbf{v}} \end{bmatrix} = \begin{bmatrix} 0 & \mathbf{I}_n \\ -\mathbf{I}_n & 0 \end{bmatrix} \begin{bmatrix} -\mathbf{A}\mathbf{u} + \mathbf{g}(\mathbf{u}) \\ \mathbf{v} \end{bmatrix}, \tag{5.12}$$

where $\mathbf{A}$ is a discrete, scaled, one-dimensional second order differential operator. The discrete Hamiltonian is given by $H\Delta x$ with

$$H(t) = \frac{1}{2}\mathbf{v}^\top \mathbf{v} - \frac{1}{2}\mathbf{u}^\top \mathbf{A}\mathbf{u} + \mathbf{c}^\top \mathbf{G}(\mathbf{u}), \tag{5.13}$$

where $\mathbf{c}$ is a vector consisting of all ones and $\mathbf{c}^\top \mathbf{G}(\mathbf{u})$ corresponds to the discretization of the integration of $G(u)$.

We will focus on the nonlinear case in which $g(u) = \sin(u)$ and $[\mathbf{G}(\mathbf{u})]_i = 1 - \cos(u_i)$ and $[\mathbf{g}(\mathbf{u})]_i = \sin(u_i)$ for $i = 0, \ldots, N-1$. For these experiments, we chose $c = 0.1$, $l = 1$. The initial condition satisfies $u(0) = f(s(x))$ and $\dot{u}(0) = 0$ where $f(s)$ is a cubic spline function defined as

$$f(s) = \begin{cases} 1 - \frac{3}{2}s^2 + \frac{3}{4}s^3 & 0 \le s \le 1 \\ \frac{1}{4}(2-s)^3 & 1 < s \le 2 \\ 0 & s \ge 2 \end{cases}$$

where $s(x) = 10|x - \frac{1}{2}|$.

5.2.1 SP-DEIM with standard basis

The nonlinear model, denoted by SP-DEIM-1, has the following form:

$$\begin{bmatrix} \dot{\mathbf{a}} \\ \dot{\mathbf{b}} \end{bmatrix} = \begin{bmatrix} 0 & \boldsymbol{\Phi}_u^\top \boldsymbol{\Phi}_v \\ -\boldsymbol{\Phi}_v^\top \boldsymbol{\Phi}_u & 0 \end{bmatrix} \begin{bmatrix} -\mathbf{A}_r \mathbf{a} + \boldsymbol{\Phi}_u^\top \mathbf{g}(\boldsymbol{\Phi}_u \mathbf{a}) \mathbb{P}^\top C \\ \mathbf{b} \end{bmatrix} \tag{5.14}$$

After discretization, we have

$$\begin{bmatrix} \frac{\mathbf{a}^{k+1}-\mathbf{a}^k}{\Delta t} \\ \frac{\mathbf{b}^{k+1}-\mathbf{b}^k}{\Delta t} \end{bmatrix} = \begin{bmatrix} 0 & \boldsymbol{\Phi}_u^\top \boldsymbol{\Phi}_v \\ -\boldsymbol{\Phi}_v^\top \boldsymbol{\Phi}_u & 0 \end{bmatrix} \begin{bmatrix} -\mathbf{A}_r \frac{\mathbf{a}^{k+1}+\mathbf{a}^k}{2} + \boldsymbol{\Phi}_u^\top \mathbf{g}(\boldsymbol{\Phi}_u \frac{\mathbf{a}^{k+1}+\mathbf{a}^k}{2}) \mathbb{P}^\top C \\ \frac{\mathbf{b}^{k+1}+\mathbf{b}^k}{2} \end{bmatrix}, \tag{5.15}$$

where the initial conditions are $\mathbf{a}^0 = \boldsymbol{\Phi}_u^\top \mathbf{u}_0$ and $\mathbf{b}^0 = \boldsymbol{\Phi}_v^\top \mathbf{v}_0$.

For $r = 5$, the computation takes 0.58568 seconds, while for $r = 20$ it is found to take 0.88025 seconds. The results are presented in Figures 5.1, 5.2 and 5.3 below. It is observed that the Hamiltonian approximation error is on the order of 10^{-3} when $r = 5$ and decreases to 10^{-7} when $r = 20$. The corresponding maximum errors of the reduced order simulations are $\varepsilon_\infty = 0.284374$ for $r = 5$, and $\varepsilon_\infty = 0.0082983$ for $r = 20$, which shows a significant improvement. It is noted that the maximum error values appear to be similar to those obtained by the SP-ROM without using the DEIM.

5.2.2 SP-DEIM with shifted basis

In attempt to improve upon the discrete Hamiltonian, the POD basis is generated from shifted snapshots and the DEIM basis from shifted nonlinear snapshots. This model, denoted by the SP-DEIM-2, has the following form:

$$\begin{bmatrix} \dot{\mathbf{a}} \\ \dot{\mathbf{b}} \end{bmatrix} = \begin{bmatrix} 0 & \boldsymbol{\Phi}_u^\top \boldsymbol{\Phi}_v \\ -\boldsymbol{\Phi}_v^\top \boldsymbol{\Phi}_u & 0 \end{bmatrix} \begin{bmatrix} -\mathbf{A}_r \mathbf{a} - \boldsymbol{\Phi}_u^\top \mathbf{A} \mathbf{u}_0 + \boldsymbol{\Phi}_u^\top \mathbf{g}(\boldsymbol{\Phi}_u \mathbf{a} + \mathbf{u_0}) \mathbb{P}^\top C \\ \mathbf{b} + \boldsymbol{\Phi}_v^\top \mathbf{v}_0 \end{bmatrix}. \tag{5.16}$$

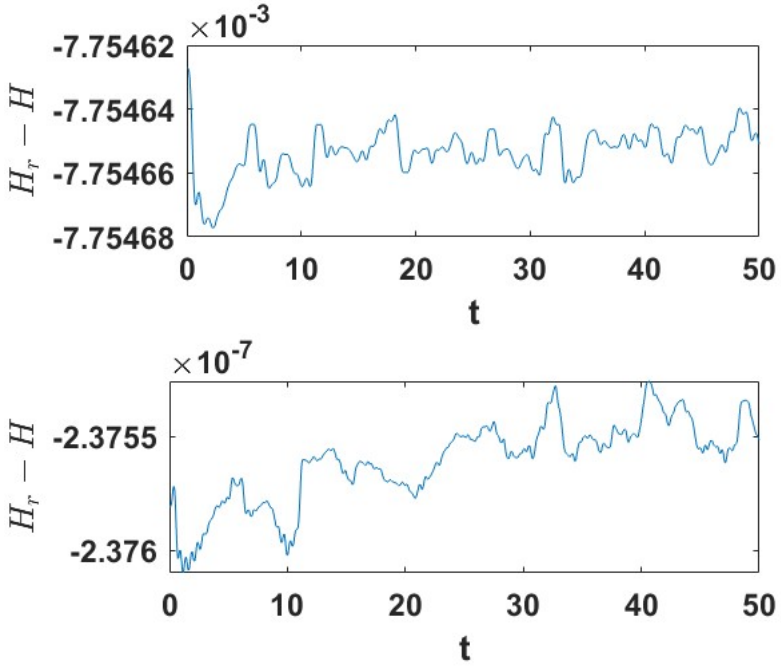

Figure 5.1 SP-DEIM-1: Hamiltonian errors for $r = 5$ (top) and $r = 20$ (bottom).

The discretization leads to the following system:

$$\begin{bmatrix} \frac{\mathbf{a}^{k+1}-\mathbf{a}^k}{\Delta t} \\ \frac{\mathbf{b}^{k+1}-\mathbf{b}^k}{\Delta t} \end{bmatrix} = \begin{bmatrix} 0 & \boldsymbol{\Phi}_u^\top \boldsymbol{\Phi}_v \\ -\boldsymbol{\Phi}_v^\top \boldsymbol{\Phi}_u & 0 \end{bmatrix} \begin{bmatrix} -\mathbf{A}_r \frac{\mathbf{a}^{k+1}+\mathbf{a}^k}{2} - \boldsymbol{\Phi}_u^\top \mathbf{A}\mathbf{u}_0 + \boldsymbol{\Phi}_u^\top \mathbf{g}(\boldsymbol{\Phi}_u \frac{\mathbf{a}^{k+1}+\mathbf{a}^k}{2}) \mathbb{P}^\top C \\ \frac{\mathbf{b}^{k+1}+\mathbf{b}^k}{2} + \boldsymbol{\Phi}_v^\top \mathbf{v}_0 \end{bmatrix}, \tag{5.17}$$

where the initial conditions are $\mathbf{a}^0 = \mathbf{0}$ and $\mathbf{b}^0 = \mathbf{0}$.

Again, the models were run for both $r = 5$ and $r = 20$. The computation times were not significantly increased for either simulation, with the corresponding times of 0.60806 and 0.90458 seconds, while the Hamiltonian approximation errors decrease to the order of 10^{-8} and 10^{-11}, respectively. The associated maximum errors were found to be $\varepsilon_\infty = 0.44364$ and $\varepsilon_\infty = 0.011517$. It is noted here that these errors are larger than those obtained by the SP-POD-2 without using the DEIM. These errors can be further improved by increasing the number of DEIM basis and interpolation points. The results of the SP-DEIM-2 model are presented in the Figures 5.4, 5.5

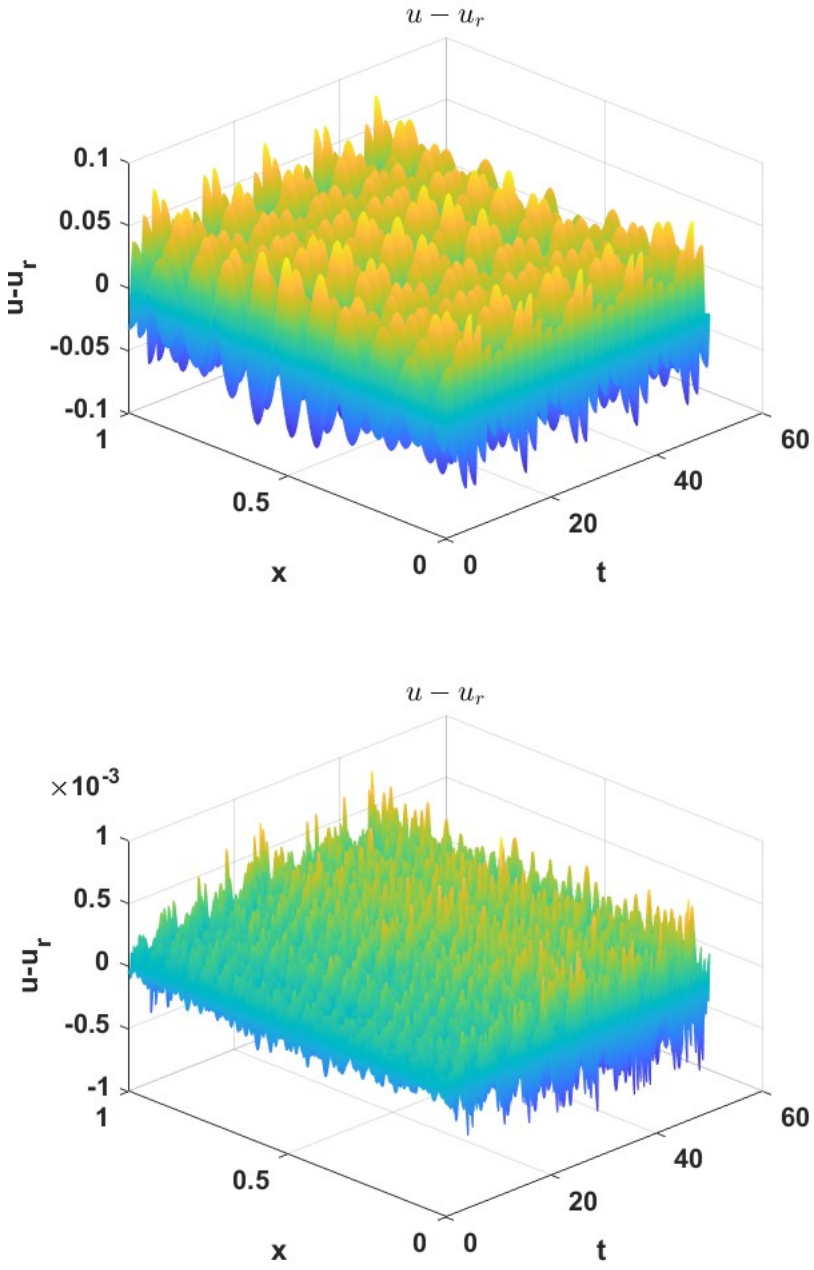

Figure 5.2 SP-DEIM-1: u error plots for $r = 5$ (top) and $r = 20$ (bottom).

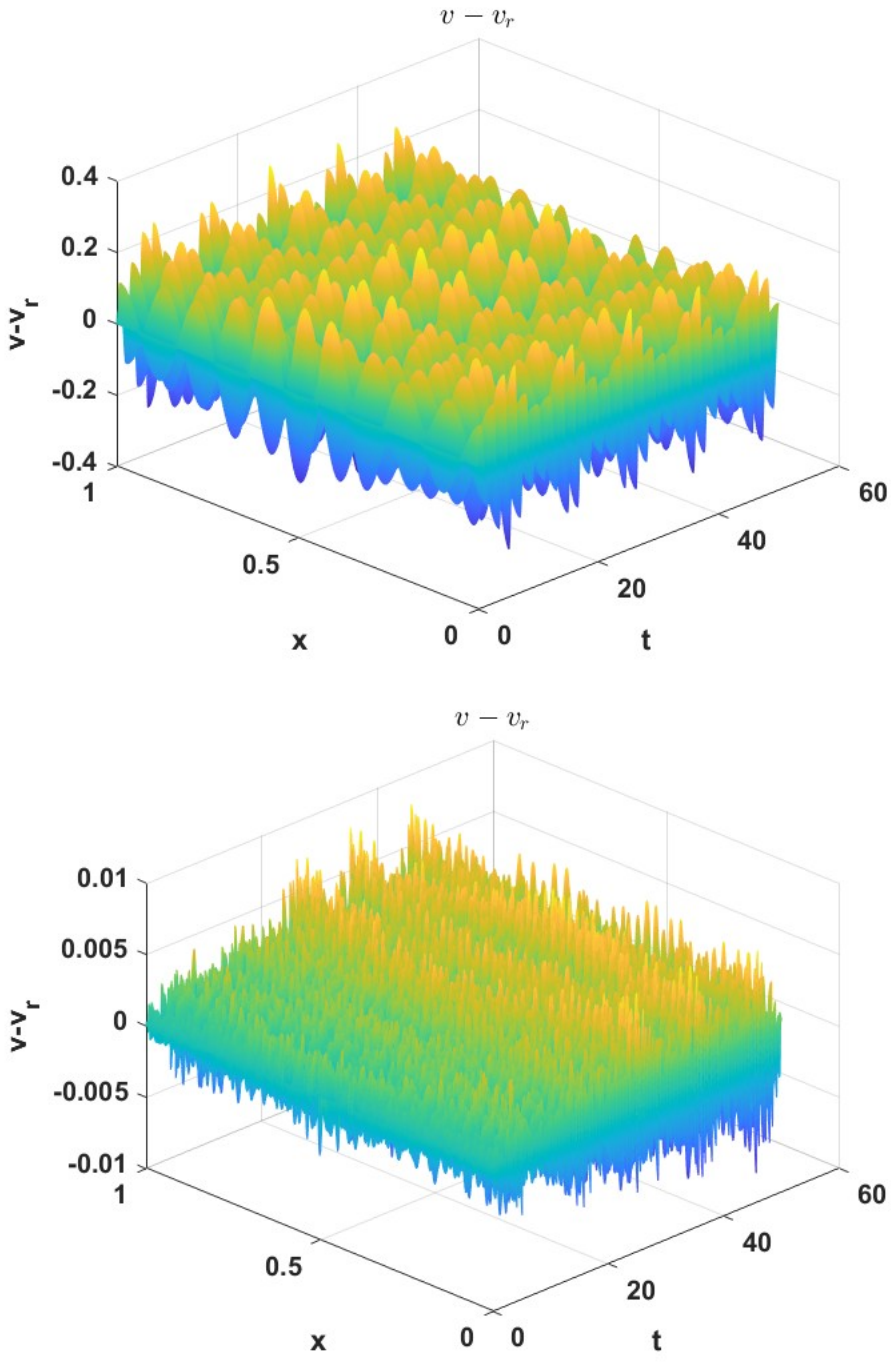

Figure 5.3 SP-DEIM-1: v error plots for $r = 5$ (top) and $r = 20$ (bottom).

and 5.6 and show how the model is able to preserve the discrete Hamiltonian.

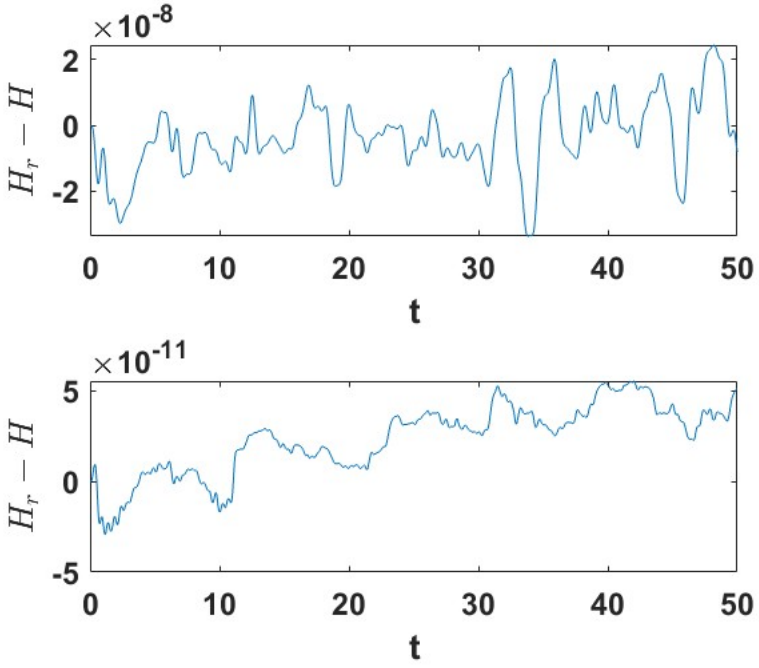

Figure 5.4 SP-DEIM-2: Hamiltonian errors for $r = 5$ (top) and $r = 20$ (bottom).

Therefore, the structure-preserving DEIM modes with shifted snapshot bases are able to preserve the energy of the systems and therefore results in better Hamiltonian approximations than other ROMs. In addition, the use of SP-DEIM models reduces the computation time significantly.

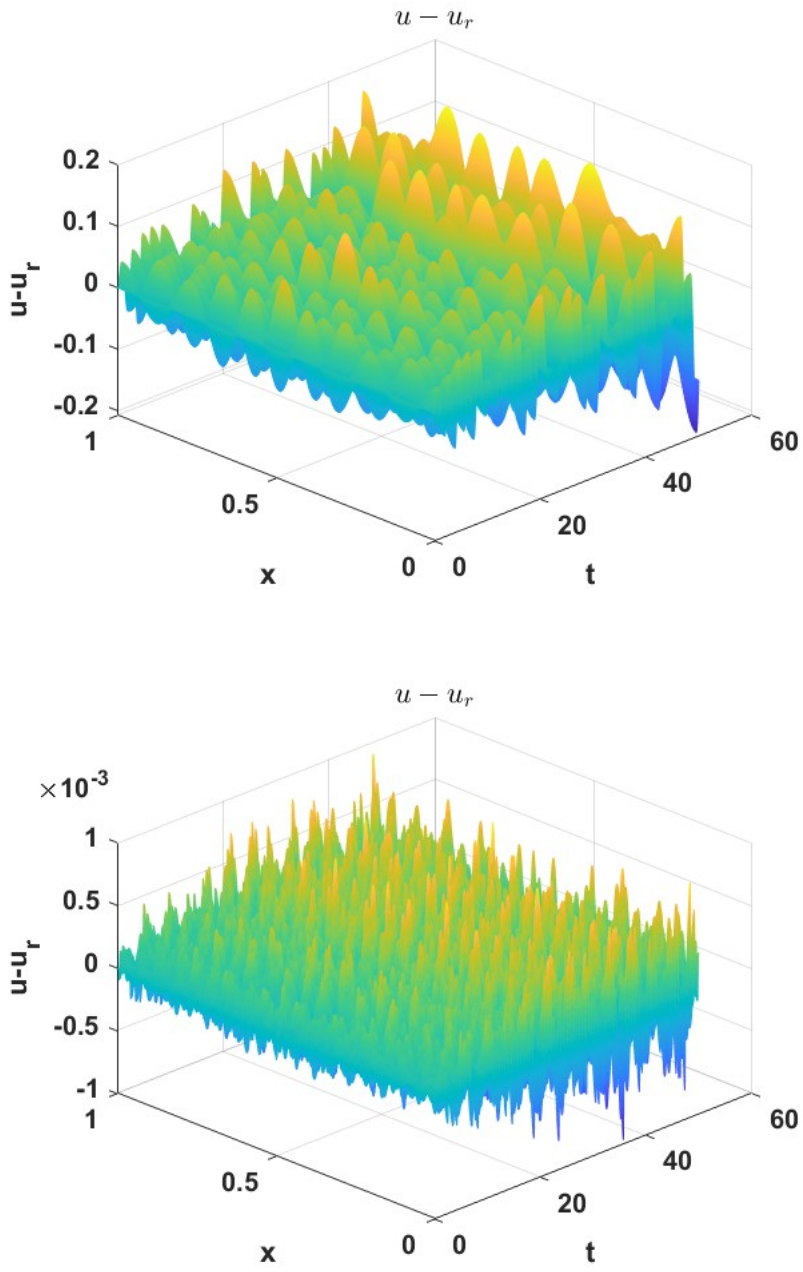

Figure 5.5 SP-DEIM-2: u error plots for $r = 5$ (top) and $r = 20$ (bottom).

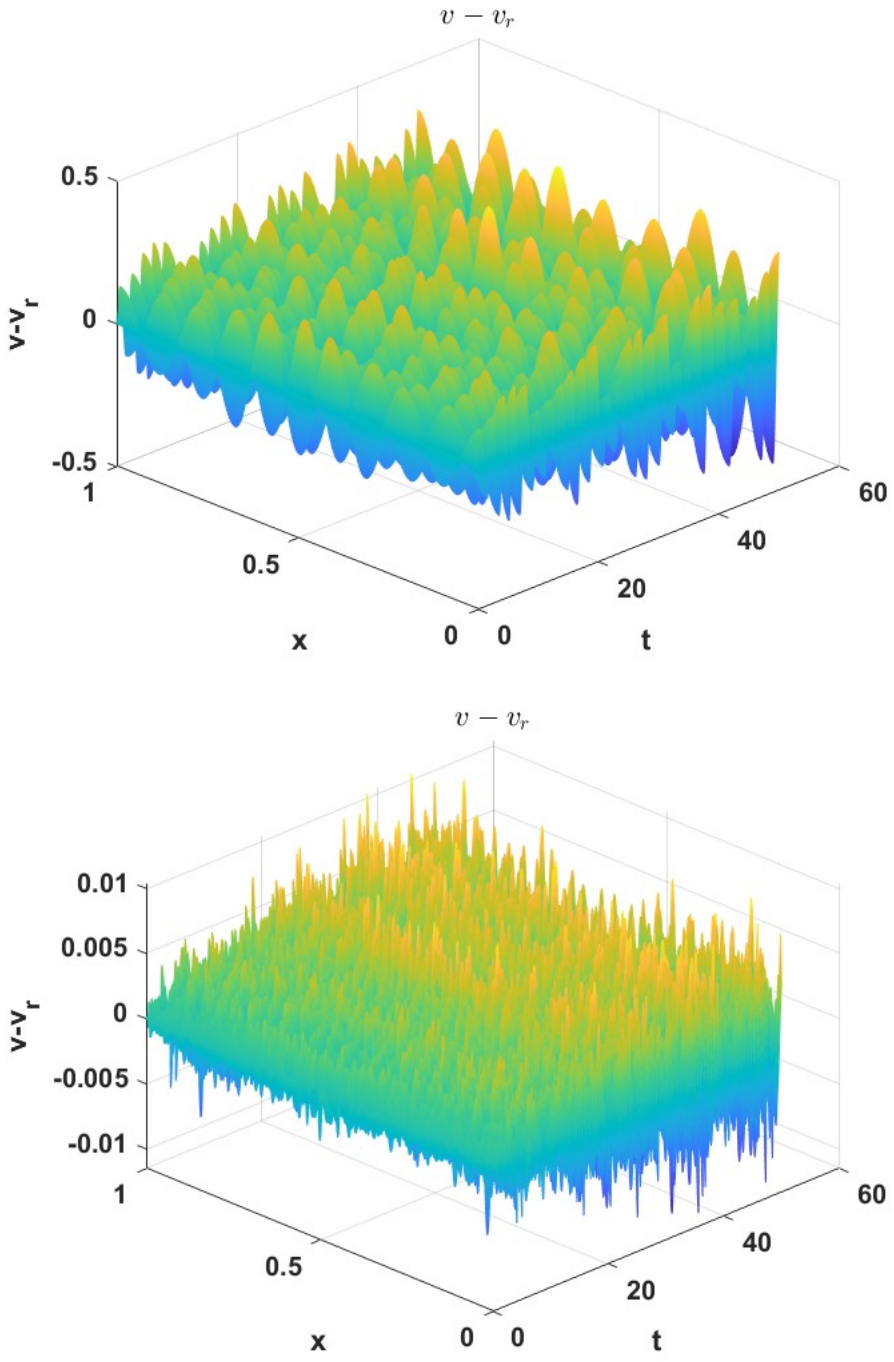

Figure 5.6 SP-DEIM-2: v error plots for $r = 5$ (top) and $r = 20$ (bottom).

Chapter 6

Conclusion

One of the defining characteristics of a conservative Hamiltonian system is to preserve the Hamiltonian function. To develop an efficient surrogate of the full order model, the proper orthogonal decomposition method could be used. However, it can not properly preserve the geometric structure of the system. Therefore, the structure-preserving ROMs (SP-ROMs) have been designed. By investigating the performance of such ROMs on a wave equation, it is shown that using the POD basis created from shifted snapshots could produce an accurate Hamiltonian approximation and accurate solutions to the system. While the SP-ROMs yield good numerical performances, when the gradient of the Hamiltonian has non-polynomial nonlinearities, the computational complexity is still high. This work considers the combination of the DEIM with the SP-ROMs and demonstrates its efficacy in improving online efficiency while maintaining accurate approximations. Numerical experiments illustrate the capability of each discussed approach. Future work may extend the discussed approaches to dissipative Hamiltonian systems or port-Hamiltonian systems. Another possible research direction is to develop data-driven structure-preserving ROMs.

Bibliography

[1] Andrea Manzoni Alfio Quarteroni and Federico Negri. In: *Reduced Basis Methods for Partial Differential Equations*. Springer Cham, 2016. DOI: https://doi.org/10.1007/978-3-319-15431-2.

[2] Neveen Ali Eshtewy and Lena Scholz. "Model Reduction for Kinetic Models of Biological Systems". In: *Symmetry* 12.5 (2020). ISSN: 2073-8994. DOI: 10.3390/sym12050863. URL: https://www.mdpi.com/2073-8994/12/5/863.

[3] David Amsallem and Charbel Farhat. "Interpolation Method for Adapting Reduced-Order Models and Application to Aeroelasticity". In: *AIAA Journal* 46.7 (2008), pp. 1803–1813. DOI: 10.2514/1.35374. eprint: https://doi.org/10.2514/1.35374. URL: https://doi.org/10.2514/1.35374.

[4] David Amsallem and Bernard Haasdonk. "PEBL-ROM: Projection-error based local reduced-order models". In: *Advanced Modeling and Simulation in Engineering Sciences* 3 (1 2016). URL: https://doi.org/10.1186/s40323-016-0059-7.

[5] A. C. Antoulas, I. V. Gosea, and A. C. Ionita. "Model Reduction of Bilinear Systems in the Loewner Framework". In: *SIAM Journal on Scientific Computing* 38.5 (2016), B889–B916. DOI: 10.1137/15M1041432. eprint: https://doi.org/10.1137/15M1041432. URL: https://doi.org/10.1137/15M1041432.

[6] Matthew Franklin Barone et al. "Reduced order modeling of fluid/structure interaction." In: (Nov. 2009). DOI: 10.2172/974411. URL: https://www.osti.gov/biblio/974411.

[7] Peter Benner, Serkan Gugercin, and Karen Willcox. "A Survey of Projection-Based Model Reduction Methods for Parametric Dynamical Systems". In: *SIAM Review* 57.4 (2015), pp. 483–531. DOI: 10.1137/130932715. eprint: https://doi.org/10.1137/130932715. URL: https://doi.org/10.1137/130932715.

[8] Peter Benner et al. "Operator inference for non-intrusive model reduction of systems with non-polynomial nonlinear terms". In: *Computer Methods in Applied Mechanics and Engineering* 372 (2020), p. 113433. ISSN: 0045-7825. DOI:

https://doi.org/10.1016/j.cma.2020.113433. URL: https://www.sciencedirect.com/science/article/pii/S0045782520306186.

[9] Thomas Bewley, Paolo Luchini, and Jan Pralits. "Methods for solution of large optimal control problems that bypass open-loop model reduction". In: *Meccanica* 51 (12 2016). DOI: 10.1007/s11012-016-0547-3. URL: https://doi.org/10.1007/s11012-016-0547-3.

[10] Trevor J. Blanc, Matthew R. Jones, and Steven E. Gorrell. "Reduced-Order Modeling of Conjugate Heat Transfer Processes". In: *Journal of Heat Transfer* 138.5 (Feb. 2016). 051703. ISSN: 0022-1481. DOI: 10.1115/1.4032453. eprint: https://asmedigitalcollection.asme.org/heattransfer/article-pdf/138/5/051703/6211779/ht_138_05_051703.pdf. URL: https://doi.org/10.1115/1.4032453.

[11] Steven L. Brunton and J. Nathan Kutz. "Reduced Order Models (ROMs)". In: *Data-Driven Science and Engineering: Machine Learning, Dynamical Systems, and Control*. Cambridge University Press, 2019. DOI: 10.1017/9781108380690.012.

[12] Tan Bui-Thanh, Karen E. Willcox, and Omar Ghattas. "Parametric reduced-order models for probabilistic analysis of unsteady aerodynamic applications". In: *AIAA Journal* 46 (2007), pp. 2520–2529.

[13] E. Celledoni et al. "Preserving energy resp. dissipation in numerical PDEs using the "Average Vector Field" method". In: *Journal of Computational Physics* 231.20 (Aug. 2012), pp. 6770–6789. DOI: 10.1016/j.jcp.2012.06.022. URL: https://doi.org/10.1016%2Fj.jcp.2012.06.022.

[14] S. Chaturantabut, C. Beattie, and S. Gugercin. "Structure-Preserving Model Reduction for Nonlinear Port-Hamiltonian Systems". In: *SIAM Journal on Scientific Computing* 38.5 (2016), B837–B865. DOI: 10.1137/15M1055085. eprint: https://doi.org/10.1137/15M1055085. URL: https://doi.org/10.1137/15M1055085.

[15] Saifon Chaturantabut and Danny C. Sorensen. "A State Space Error Estimate for POD-DEIM Nonlinear Model Reduction". In: *SIAM Journal on Numerical Analysis* 50.1 (2012), pp. 46–63. DOI: 10.1137/110822724. eprint: https://doi.org/10.1137/110822724. URL: https://doi.org/10.1137/110822724.

[16] Jan L. Cieśliński. "Improving the accuracy of the AVF method". In: *Journal of Computational and Applied Mathematics* 259 (2014). Proceedings of the Sixteenth International Congress on Computational and Applied Mathematics (ICCAM-2012), Ghent, Belgium, 9-13 July, 2012, pp. 233–243. ISSN: 0377-

0427. DOI: https://doi.org/10.1016/j.cam.2013.08.008. URL: https://www.sciencedirect.com/science/article/pii/S0377042713004135.

[17] Luca Daniel et al. "A Multiparameter Moment-Matching Model-Reduction Approach for Generating Geometrically Parameterized Interconect Performance Models". In: *IEEE Journal* 23.5 (2004), pp. 678–693. URL: http://www.mit.edu/~dluca/publications/daniel_TRANS_2004_pmor.pdf.

[18] Z. Drmač, S. Gugercin, and C. Beattie. "Quadrature-Based Vector Fitting for Discretized $\mathcal{H}_2$ Approximation". In: *SIAM Journal on Scientific Computing* 37.2 (Jan. 2015), A625–A652. ISSN: 1095-7197. DOI: 10.1137/140961511. URL: http://dx.doi.org/10.1137/140961511.

[19] Christian Lubich Ernst Hairer Gerhard Wanner. In: *Geometric Numerical Integration*. Springer Berlin, Heidelberg, 2006. DOI: https://doi.org/10.1007/3-540-30666-8.

[20] Erwan Faou, Ernst Hairer, and Truong-Linh Pham. "Energy Conservation with Non-Symplectic Methods: Examples and Counter-Examples". In: *BIT Numerical Mathematics* 44 (4 2004).

[21] Nicholas Galioto and Alex A. Gorodetsky. "Bayesian Identification of Hamiltonian Dynamics from Symplectic Data". In: *2020 59th IEEE Conference on Decision and Control (CDC)*. 2020, pp. 1190–1195. DOI: 10.1109/CDC42340.2020.9303852.

[22] Yuezheng Gong, Qi Wang, and Zhu Wang. "Structure-preserving Galerkin POD reduced-order modeling of Hamiltonian systems". In: *Computer Methods in Applied Mechanics and Engineering* 315 (Mar. 2017), pp. 780–798. ISSN: 0045-7825. DOI: 10.1016/j.cma.2016.11.016. URL: http://dx.doi.org/10.1016/j.cma.2016.11.016.

[23] Ion Victor Gosea and Athanasios C. Antoulas. "Data-driven model order reduction of quadratic-bilinear systems". In: *Numerical Linear Algebra with Applications* 25.6 (2018). e2200 nla.2200, e2200. DOI: https://doi.org/10.1002/nla.2200. eprint: https://onlinelibrary.wiley.com/doi/pdf/10.1002/nla.2200. URL: https://onlinelibrary.wiley.com/doi/abs/10.1002/nla.2200.

[24] Samuel Greydanus, Misko Dzamba, and Jason Yosinski. "Hamiltonian Neural Networks". In: ed. by H. Wallach et al. Vol. 32. Curran Associates, Inc., 2019. URL: https://proceedings.neurips.cc/paper/2019/file/26cd8ecadce0d4efd6cc8a8725cbdPaper.pdf.

[25] Martin Hess and Peter Benner. "A reduced basis method for microwave semiconductor devices with geometric variations". In: *COMPEL: The International Journal for Computation and Mathematics in Electrical and Electronic Engineering* 33.4 (2014), pp. 1071–1081. DOI: 10.1108/COMPEL-12-2012-0377. URL: https://doi.org/10.1108/COMPEL-12-2012-0377.

[26] H. Hotelling. "Analysis of a complex of statistical variables into principal components". In: *Journal of Educational Psychology* 24.6 (1933), pp. 417–441. DOI: 10.1037/h0071325.

[27] Baohui Hou and Dong Liang. "Energy-preserving time high-order AVF compact finite difference schemes for nonlinear wave equations with variable coefficients". In: *Journal of Computational Physics* 421 (2020), p. 109738. ISSN: 0021-9991. DOI: https://doi.org/10.1016/j.jcp.2020.109738. URL: https://www.sciencedirect.com/science/article/pii/S002199912030512X.

[28] Gianluigi Rozza Jan S Hesthaven and Benjamin Stamm. In: *Certified Reduced Basis Methods for Parametrized Partial Differential Equations*. Springer Cham, 2016. DOI: https://doi.org/10.1007/978-3-319-22470-1.

[29] Pengzhan Jin et al. "SympNets: Intrinsic structure-preserving symplectic networks for identifying Hamiltonian systems". In: *Neural Networks* 132 (2020), pp. 166–179. ISSN: 0893-6080. DOI: https://doi.org/10.1016/j.neunet.2020.08.017. URL: https://www.sciencedirect.com/science/article/pii/S0893608020303063.

[30] Ian Jolliffe. "Principal Component Analysis". In: (2005). URL: https://doi.org/10.1002/0470013192.bsa501.

[31] Bülent Karasözen and Murat Uzunca. "Energy preserving model order reduction of the nonlinear Schrödinger equation". In: *Advances in Computational Mathematics* 44 (6 2018). DOI: 10.1007/s10444-018-9593-9. URL: https://doi.org/10.1007/s10444-018-9593-9.

[32] D. Kosambi. *Statistics in function space*. 1943.

[33] Karl Kunisch and Stefan Volkwein. "Proper orthogonal decomposition for optimality systems". In: *ESAIM: Mathematical Modelling and Numerical Analysis - Modélisation Mathématique et Analyse Numérique* 42.1 (2008), pp. 1–23. DOI: 10.1051/m2an:2007054. URL: http://www.numdam.org/articles/10.1051/m2an:2007054/.

[34] Haochen Li, Yushun Wang, and Qin Mengzhao. "A Sixth order Averaged Vector Field Method". In: *Journal of Computational Mathematics* 34 (Dec. 2014). DOI: 10.4208/jcm.1601-m2015-0265.

[35] Xin Li, Peng Li, and L. T. Pileggi. "Parameterized Interconnect Order Reduction with Explicit-and-Implicit Multi-Parameter Moment Matching for Inter/Intra-Die Variations". In: *Proceedings of the 2005 IEEE/ACM International Conference on Computer-Aided Design*. ICCAD '05. San Jose, CA: IEEE Computer Society, 2005, pp. 806–812. ISBN: 078039254X.

[36] M. Loéve. *Probability Theory*. D. Van Nostrand, 1955.

[37] J. Lumley. *The Structure of Inhomogeneous Turbulent Flow*. 1967.

[38] Zhanhua Ma, Sunil Ahuja, and Clarence W. Rowley. "Reduced-order models for control of fluids using the eigensystem realization algorithm". In: *Theoretical and Computational Fluid Dynamics* 25 (2011), pp. 233–247. DOI: 10.1007/s00162-010-0184-8. URL: https://doi.org/10.1007/s00162-010-0184-8.

[39] Robert I. McLachlan, G. R. W. Quispel, and Nicolas Robidoux. "Geometric Integration Using Discrete Gradients". In: *Philosophical Transactions: Mathematical, Physical and Engineering Sciences* 357.1754 (1999), pp. 1021–1045. ISSN: 1364503X. URL: http://www.jstor.org/stable/55188 (visited on 07/06/2022).

[40] Yuto Miyatake. "Structure-preserving model reduction for dynamical systems with a first integral". In: *Japan Journal of Industrial and Applied Mathematics* (2019).

[41] B. Moore. "Principal component analysis in linear systems: Controllability, observability, and model reduction". In: *IEEE Transactions on Automatic Control* 26.1 (1981), pp. 17–32. DOI: 10.1109/TAC.1981.1102568.

[42] G. North et al. "Sampling Errors in the Estimation of Empirical Orthogonal Functions". In: *Monthly Weather Review* (1982).

[43] Peter J. Olver. *Applications of Lie Groups to Differential Equations*. 1993. DOI: https://doi.org/10.1007/978-1-4612-4350-2.

[44] Benjamin Peherstorfer. "Sampling Low-Dimensional Markovian Dynamics for Preasymptotically Recovering Reduced Models from Data with Operator Inference". In: *SIAM Journal on Scientific Computing* 42.5 (2020), A3489–A3515. DOI: 10.1137/19M1292448. eprint: https://doi.org/10.1137/19M1292448. URL: https://doi.org/10.1137/19M1292448.

[45] Benjamin Peherstorfer and Karen Willcox. "Data-driven operator inference for nonintrusive projection-based model reduction". In: *Computer Methods in Applied Mechanics and Engineering* 306 (2016), pp. 196–215. ISSN: 0045-7825.

DOI: https://doi.org/10.1016/j.cma.2016.03.025. URL: https://www.sciencedirect.com/science/article/pii/S0045782516301104.

[46] Elizabeth Qian et al. "A certifies trust region reduced basis approach to PDE-constrained optimization". In: *SIAM Journal on Scientific Computing* 39.5 (2017), S434–60. URL: https://dspace.mit.edu/handle/1721.1/116912.

[47] G R W Quispel and D I McLaren. "A new class of energy-preserving numerical integration methods". In: *Journal of Physics A: Mathematical and Theoretical* 41.4 (Jan. 2008), p. 045206. DOI: 10.1088/1751-8113/41/4/045206. URL: https://doi.org/10.1088/1751-8113/41/4/045206.

[48] Junior Rojas, Tiantian Liu, and Ladislav Kavan. "Average Vector Field Integration for St. Venant-Kirchhoff Deformable Models". In: *IEEE Transactions on Visualization and Computer Graphics* (2018).

[49] C. W. Rowley. "MODEL REDUCTION FOR FLUIDS, USING BALANCED PROPER ORTHOGONAL DECOMPOSITION". In: *International Journal of Bifurcation and Chaos* 15.03 (). DOI: https://doi.org/10.1142/S0218127405012429.

[50] J.M. Sanz-Serna. "Solving Numerically Hamiltonian Systems". In: (1995). URL: https://doi.org/10.1007/978-3-0348-9078-6%5C_143.

[51] Harsh Sharma, Zhu Wang, and Boris Kramer. *Hamiltonian Operator Inference: Physics-preserving Learning of Reduced-order Models for Canonical Hamiltonian Systems*. 2021. arXiv: 2107.12996 [math.NA].

[52] Renee Swischuk et al. "Learning Physics-Based Reduced-Order Models for a Single-Injector Combustion Process". In: 58.6 (2020). DOI: https://doi.org/10.2514/1.J058943.

[53] Wayne Isaac Tan Uy and Benjamin Peherstorfer. "TI - Operator Inference of Non-Markovian Terms for Learning Reduced Models from Partially Observed State Trajectories". In: *Journal of Scientific Computing* 88 (3 2021). DOI: 10.1007/s10915-021-01580-2. URL: https://doi.org/10.1007/s10915-021-01580-2.

[54] Hui Wang, Zhenshan Li, and Ningsheng Cai. "Reduced-order model for redox kinetics of oxygen carrier in chemical looping combustion". In: *Proceedings of the Combustion Institute* 38.4 (2021), pp. 5271–5279. ISSN: 1540-7489. DOI: https://doi.org/10.1016/j.proci.2020.08.002. URL: https://www.sciencedirect.com/science/article/pii/S1540748920303011.

[55] Zhu Wang. *Structure-Preserving Galerkin POD-DEIM Reduced-Order Modeling of Hamiltonian Systems*. 2021. DOI: 10.48550/ARXIV.2103.00388. URL: https://arxiv.org/abs/2103.00388.

[56] Zhu Wang, Brian McBee, and Traian Iliescu. "Approximate partitioned method of snapshots for POD". In: *Journal of Computational and Applied Mathematics* 307 (2016). 1st Annual Meeting of SIAM Central States Section, April 11–12, 2015, pp. 374–384. ISSN: 0377-0427. DOI: https://doi.org/10.1016/j.cam.2015.11.023. URL: https://www.sciencedirect.com/science/article/pii/S0377042715005774.